MASARYKOVA UNIVERZITA
PŘÍRODOVĚDECKÁ FAKULTA
ÚSTAV TEORETICKÉ FYZIKY A ASTROFYZIKY

Diplomová práce

BRNO 2015 **MICHAL PRIŠEGEN**

MASARYKOVA UNIVERZITA
PŘÍRODOVĚDECKÁ FAKULTA
ÚSTAV TEORETICKÉ FYZIKY A ASTROFYZIKY

Astrofyzika čelních rázových vln

Diplomová práce

Michal Prišegen

Vedoucí práce: Mgr. Filip Hroch, Ph.D. Brno 2015

Bibliografický záznam

Autor:	Bc. Michal Prišegen Přírodovědecká fakulta, Masarykova univerzita Ústav teoretické fyziky a astrofyziky

Název práce:	Astrofyzika čelních rázových vln
Studijní program:	Teoretická fyzika a astrofyzika
Studijní obor:	Astrofyzika
Vedoucí práce:	Mgr. Filip Hroch, Ph.D.
Akademický rok:	2014/2015
Počet stran:	xiv + 77
Klíčová slova:	rázová vlna; Spitzer; WISE; Herschel; Chandra

Bibliographic Entry

Author:	Bc. Michal Prišegen Faculty of Science, Masaryk University Department of theoretical physics and astrophysics
Title of Thesis:	On astrophysics of bow-shocks
Degree Programme:	Theoretical physics and astrophysics
Field of Study:	Astrophysics
Supervisor:	Mgr. Filip Hroch, Ph.D.
Academic Year:	2014/2015
Number of Pages:	xiv + 77
Keywords:	bow shock; Spitzer; WISE; Herschel; Chandra

Abstrakt

V této diplomové práci se věnujeme studiu čelních rázových vln v okolí hvězd raných spektrálních typů. O čelných rázových vlnách se zatím ví velmi málo, jelikož byly detekované teprve před pár lety a zahrnují exotickou fyziku v exotických podmínkách. Tato práce se zabývá několika zatím nevyřešenými problémy z oblasti astrofyziky čelních rázových vln, zejména z oblasti jejich morfologie a vyzařování v rentgenové a daleké infračervené oblasti. Zabýváme se odchylkami pozorovaných tvarů čelných rázových vln od jejich teoretických tvarů, potenciálním využití detektoru PACS pro studium těchto objektů a nacházíme kandidáta pro čelnou rázovou vlnu okolo hvězdy 2MASS J17222408-3708484. Zabýváme se též nepřítomností rentgenové emise z čelných rázových vln okolo hvězd v našem vzorku a navrhujeme jednoduchou metodu, jak určit prostorovou pekuliární rychlost hvězdy, která formuje čelní rázovou vlnu a Strömgrenovu sféru.

Abstract

In this thesis we study stellar bow shocks around early-type stars. These objects have been known only for a couple of years and involve exotic physics so they are still poorly understood. This work adresses some of the unresolved problems in bow shock astrophysics, particularly in the areas involving their morphologies, far-infrared and X-ray emission. We discuss the deviations of the observed bow shocks from their prescribed shape, discuss the untapped potential of the Herschel PACS data for bow shock research and detect a bow shock candidate associated with 2MASS J17222408-3708484. We also note the non-detection of X-ray radiation from the bow shocks in our sample and propose a simple method that can be used to determine peculiar velocities of the stars having both stellar bow shocks and Strömgren spheres.

Masarykova univerzita

Přírodovědecká fakulta

ZADÁNÍ DIPLOMOVÉ PRÁCE

Student : **Bc. Michal Prišegen, učo 324172**
Studijní program : **Fyzika**
Studijní obor : **Teoretická fyzika a astrofyzika**

Ředitel Ústavu teoretické fyziky a astrofyziky PřF MU Vám ve smyslu Studijního a zkušebního řádu MU určuje diplomovou práci s tématem:

Astrofyzika čelních rázových vln

On astrophysics of bow-shocks

Zásady pro vypracování: Čelní rázové vlny (bow-shock) byly v kosmickém prostoru detekovány v nedávné minulosti flotilou astronomických infračervených družic. Jejich detekce vyžaduje velké úhlové rozlišení, citlivou aparaturu v dosud neprozkoumané části hvězdné oblohy a daném spektrálním oboru. Vycházejíce z této skutečnosti, není překvapením, že fyzikální poznání tohoto typu objektů není příliš hluboké a komplexní. Cílem této práce by mělo být detailní studium dynamiky, kinematiky a zářivých vlastností jak samotných bow-shocků tak i okolního prostředí.

Těžiště práce bude spočívat ve zpracování pozorování bow-shocků za pomocí dostupných dat ve vhodných oborech elekromagnetického spektra. K tomu by mělo být použito nejmodernějších astrofyzikálních, statistických metod a metod zpracování obrazu. Práce by měla obsahovat fyzikální interpretaci výsledků k nimž se dospělo.

Po domluvě s vedoucím DP může být DP napsána v českém, slovenském a anglickém jazyce.

Vedoucí diplomové práce : Mgr. Filip Hroch, Ph.D.
Datum zadání diplomové práce : leden 2013
Datum odevzdání diplomové práce : dle harmonogramu ak. roku 2013/2014

V Brně leden 2013

Rikard von Unge
ředitel ÚTFA

Zadání diplomové práce převzal dne:

Podpis studenta

Poděkování

I would like to extend my thanks to Mgr. Filip Hroch, mainly for his saintly patience and fruitfull discussions. This thesis would have never seen the light of the day without him.

This research has made use of the NASA/ IPAC Infrared Science Archive, which is operated by the Jet Propulsion Laboratory, California Institute of Technology, under contract with the National Aeronautics and Space Administration.

This work is based [in part] on observations made with the Spitzer Space Telescope, which is operated by the Jet Propulsion Laboratory, California Institute of Technology under a contract with NASA.

This publication makes use of data products from the Wide-field Infrared Survey Explorer, which is a joint project of the University of California, Los Angeles, and the Jet Propulsion Laboratory/California Institute of Technology, funded by the National Aeronautics and Space Administration.

Herschel is an ESA space observatory with science instruments provided by European-led Principal Investigator consortia and with important participation from NASA.

This research has made use of the SIMBAD database and the VizieR catalogue access tool, both operated at CDS, Strasbourg, France.

This publication makes use of data products from the Two Micron All Sky Survey, which is a joint project of the University of Massachusetts and the Infrared Processing and Analysis Center/California Institute of Technology, funded by the National Aeronautics and Space Administration and the National Science Foundation.

This thesis has made use of NASA's Astrophysics Data System and NASA/IPAC Extragalactic Database (NED) which is operated by the Jet Propulsion Laboratory, California Institute of Technology, under contract with the National Aeronautics and Space Administration.

This thesis has made use of data obtained from the High Energy Astrophysics Science Archive Research Center (HEASARC), provided by NASA's Goddard Space Flight Center.

This publication makes use of data products from the Two Micron All Sky Survey, which is a joint project of the University of Massachusetts and the Infrared Processing and Analysis Center/California Institute of Technology, funded by the National Aeronautics and Space Administration and the National Science Foundation.

This research has made use of the WEBDA database, operated at the Department of

Theoretical Physics and Astrophysics of the Masaryk University.

Prohlášení

Prohlašuji, že jsem svoji diplomovou práci vypracoval samostatně s využitím informačních zdrojů, které jsou v práci citovány.

Brno 7. ledna 2015 .....

Michal Prišegen

Contents

Chapter 1

Introduction

Shock waves or shocks, for short, are naturally produced within a wide range of cosmic phenomena. We encounter shocks in a sink basin when doing the dishes, when an aircraft breaks the sound barrier or in explosions. However, shock-related phenomena are not only eyecandies or harbingers of destruction. Shocks play an important part in engineering, medical therapy, remote sensing and many other areas.

However, the shocks that we encounter in space are quite different to those that we are used to seeing on Earth. The matter in space is so highly dilute that particles almost never collide with each other, so the ordinary shocks cannot form. Nevertheless, this matter is under such extreme conditions that free charges form. This allows the matter to interact together. The shocks that form when direct collisions between the particles are not in play are called collisionless shocks.

We can distinguish between two classes of collisionless shocks. In the near-Earth enviroment we can encounter nonrelativistic collisionless shocks such as the Earth's bow shock, cometary bow shocks or the heliospheric termination shock. They are accessible to us via spacecraft, which gives us an immense advantage of allowing us to perform measurements in situ the shock and the surrounding enviroment. This means we have a pretty solid understanding of these shocks as the theory can be backed up by measurements. The second class are astrophysical shocks, manifesting in various forms of electromagnetic radiation. There are none in the vicinity of Earth, so we cannot probe them directly. Despite that, we can use our understanding of nonrelativistic shocks as a guide for studying astrophysical shocks to some degree. This thesis is going to focus on a certain type of astrophysical shock, a stellar bow shock (sometimes also written as bowshock or bow-shock, depending on the publication), frequently occuring in the interstellar medium.

It is not surprising that studying bow shocks is vital to the modern astrophysics as there are a lot of questions to be answered. However, they rarely seem to get enough attention as they are quicky skimmed through in the university curriculum and the literature available on this topic is rather scarce compared to the other areas of astrophysics. There are several books dealing with the shock-related phenomena, but only the freshly-published ones even mention bow shocks, as they are relatively newly observed phenomena, even though their existence has been expected in theory for some time.

This thesis presents an attempt to collect the relevant contemporary knowledge about interstellar bow shocks. In the first parts of the thesis, I try to provide my motivation, a brief

overview of shocks in space and the physics behind bow shocks. The second, practical part of the thesis, focuses heavily on the data reduction and studying our sample of bow shocks.

1.1 Overview of parsec-scale bow shocks

Shock waves are a type of propagating wave that occur ubiquitously throughout the universe and in the more mundane everyday phenomena, as a discontinuous transition, often called the ramp, between two regions defined as upstream (unshocked) and downstream (shocked). They occur in collision-dominated media like laboratory experiments and the atmosphere, and in collisionless media such as in space, on the interplanetary to intergalactic scales.

A bow shock is a generic name given to a common type of shock. Bow shocks form when an object obstructs a supersonic flow in some medium. A planet or a comet immersed in the solar wind may serve as an example. The solar wind is highly supersonic, thus an object moving at a negligible velocity with respect to the Sun would appear to the solar wind as a ballistic object moving at a supersonic speed. The existence of the terrestrial bow shock, formed by the solar wind as it encounters Earth's magnetic field, has been predicted in the early sixties and a few years later confirmed by measurements. The bow shock around the Earth is no oddity, as bow shocks can form around other planets, not restricted to the ones orbiting the Sun. By analogy with the Solar System, it is possible that stellar winds can form bow shocks around exoplanets. The presence of bow shocks around exoplanets is one of the possible explanations for the discrepancies found in transit timings when comparing the lightcurves obtained from different bands. [1], [2]

While interplanetary bow shocks are interesting to study, this thesis is primarily concerned with interstellar bow shocks. Interstellar bow shocks may be produced by various different objects and processes. In this chapter, we are going to provide a brief introduction into kinds of bow shocks we may encounter and a summary of multiwavelength observations of these objects.

1.1.1 Wind-blowing massive stars

Stars of early spectral types moving with a high velocity with respect to the surrounding medium are the most well-known class of objects that may drive a bow shock. Stars moving with extremely high peculiar velocities (sometimes also called runaways, generally exceeding 30 $\mathrm{km\,s^{-1}}$ with regard to their local standards of rest) can be created by two main mechanisms. The first is the dynamical ejection scenario, which occurs in clusters or associations. The star acquires its high space velocity as it is ejected out from the cluster via gravitational interactions with other members of the cluster. The other one is the supernova ejection scenario. If the system was previously a binary, the supernova explosion of one of its components imparts a high velocity to the system. This explosion may or may not disrupt the binary, which depends on the initial configuration of the binary system and the type of supernova explosion (symmetric or assymetric). The effect of these two mechanisms can be stacked – a binary system may have been previously ejected from a cluster via the dynamic ejection and then one of its component may explode as a supernova, giving it a kick in a different direction. [3], [4], [5]

Figure 1.1: A bow shock generated by a runaway star ζ Oph (spectral class Be) as seen by the Spitzer Space Telescope. Blue colour represents 3.6, green 4.5 and red 24 μm light. (Image made by the author from the Spitzer data.)

There are more exotic mechanisms that may create fast-moving stars or binaries. Therebody interaction of a binary with the supermassive black hole at the Galactic center, a close encounter of a single star with a binary black hole or the interaction of an AGN jet from the central black hole with a dense molecular cloud are mechanisms that can produce stars moving with peculiar velocities exceeding several hundreds $\mathrm{km\,s^{-1}}$. Such stars are known as the hypervelocity stars. [6], [7],[8]

The combination of the high peculiar velocities and strong stellar winds of these early-type stars often give favourable conditions for bow shock formation. This structure is composed of two shocks: a forward shock in the interstellar medium (ISM) and a reverse shock in the stellar wind. The shocked material of the ISM is accumulated into a dense thin layer whereas the shocked wind forms the most extended part of the bow shock.[9]

The most common class of high-velocity objects are OB runaway stars. Being ejected from their parent clusters, their peculiar velocities are in the order of several $\mathrm{km\,s^{-1}}$. Approximately 40 % of these stars form a bow shock. Another interesting class of bow shock producers are the high-mass X-ray binaries, which are binary systems that have survived the supernova explosion of one of its components. There are several bow shocks associated with these systems as well. [10], [11]

A high peculiar velocity of the star is not a requirement for bow shock formation. Fast

moving outflows impinging on the stellar wind of a low-velocity star may also create a bow shock. For instance, high-velocity outflows driven from young star clusters by the collective effect of stellar winds can create bow shocks around stars in the cluster's vicinity. An example of this is a bow shock created around LL Ori in the M42 (the Orion Nebula). If the studied star is located far from any star-forming clusters and not affected by their outflows, the peculiar velocity of the ambient medium is negligible to the peculiar space velocity of the star, meaning that the symmetry axis of the bow shock corresponds well with the direction of stellar motion. [11]

1.1.2 Mass-ejecting giant stars

Significant mass-loss from the evolved runaway stars should provide favourable conditions for bow shock formation. Interestingly, the majority of bow shock-producing stars are either on the main sequence or are blue supergiants, while there are no Wolf-Rayet stars associated with detectable bow shocks and there are only a couple of bow shock-producing red supergiants. The different nature of the stellar wind of the evolved stars as opposed to the early type stars should give rise to bow shocks with different morphologies. However, the small sample of detected bow shocks make any comparisons inconclusive. [11], [12], [13]

1.1.3 Pulsars

Because of the kick imparted to the object by its supernova explosion, pulsars are generally born with a high peculiar space velocity of a few hundreds of $\mathrm{km\,s^{-1}}$, some objects even exceeding 1000 $\mathrm{km\,s^{-1}}$. Young pulsars are thus a population of objects with the highest peculiar velocities in the Galaxy. This high velocity allows a pulsar to eventually escape its pulsar wind nebula and travel through the shocked ejecta in the supernova remnant interior. At first, the motion of the pulsar will be subsonic in the hot, shocked gas, but by the time the pulsar approaches the edges of the supernova remnant, the sound speed should drop sufficiently for the pulsar's motion to be supersonic. Having strong winds and high velocities, pulsars may produce a pulsar wind nebula with a bow shock morphology in the supernova remnant and when they eventually escape the remnant, they may drive bow shocks through the interstellar medium. There are several known pulsar bow shocks (e.g. PSR J1549-4848, G189.22+2.90). Their interaction with the supernova remnant and their visibility in various parts of the electromagnetic spectrum make them very interesting objects to study. [14], [15], [16]

1.1.4 Outflows and jets

Stars in various stages of stellar evolution are not the only objects capable of driving bow shocks. Bow shock structures may be formed anywhere where the fast collimated outflows or expanding shells are present. A bow shock may be created as the fast-moving outflows or ejecta impinge on the surrounding dense interstellar medium or a slower moving shell. Such bowshocks are commonplace in planetary nebulae, supernova remnants and Herbig-Haro objects. A bulk motion of objects such as planetary nebulae or molecular clouds also may

give rise to bow shocks – if they are moving fast enough. An example of this may be NGC 7293 (Helix planetary nebula) that drives a bow shock as it moves through the interstellar medium at high speed. Another, a more exotic example, might be a dense, ionized cloud known as G2 moving directly toward the supermassive black hole at the Galactic center. The cloud may interact with the accretion flow of the black hole, significantly altering its dynamics. A bow shock might form as the cloud plows through the hot plasma during its pericentric passage. This should occur as this thesis is being written and the evidence of the bow shock formation currently being searched for. [17], [18], [19], [20], [22]

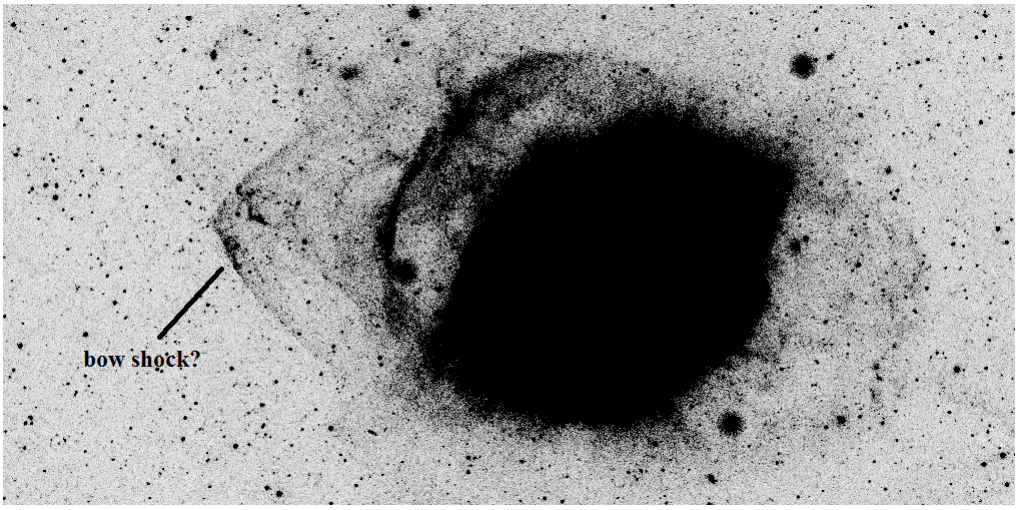

Figure 1.2: Negative grayscale presentation of the Helix planetary nebula in the GALEX NUV band (175-280 nm). There is a bow-shaped feature left of the nebula that is a probable bow shock (Image obtained via GalexView [21].)

1.2 Stellar bow shocks across the electromagnetic spectrum

Collisionless shocks are difficult to investigate in the laboratory conditions. Thus, the detections of the emission in different bands might be very important for the furthering of our understanding of the bow shock physics. Several space-based and ground-based instruments may be utilized for bow shock observations and the relevant ones will be discussed in the later chapters.

1.2.1 Infrared band

The infrared band is by far the most prolific part of the electromagnetic spectrum for bow shock observations as the most bow shocks are discovered using the infrared data. Space-based infrared missions sensitive to warm dust have been very successful in the bow shock surveys. Several bow shocks were identified in the past with the Infrared Astronomical Satellite (IRAS) and, more recently, with the Spitzer space telescope and Wide-field Infrared Survey Explorer (WISE). The observations made by the recently decommissioned

Herschel Space Observatory, operating in the longer wavelengths than the previous two missions, may also prove to be useful for the bow shock astrophysics. It is likely that many more bow shocks await discovery in the archival data accumulated by these missions.

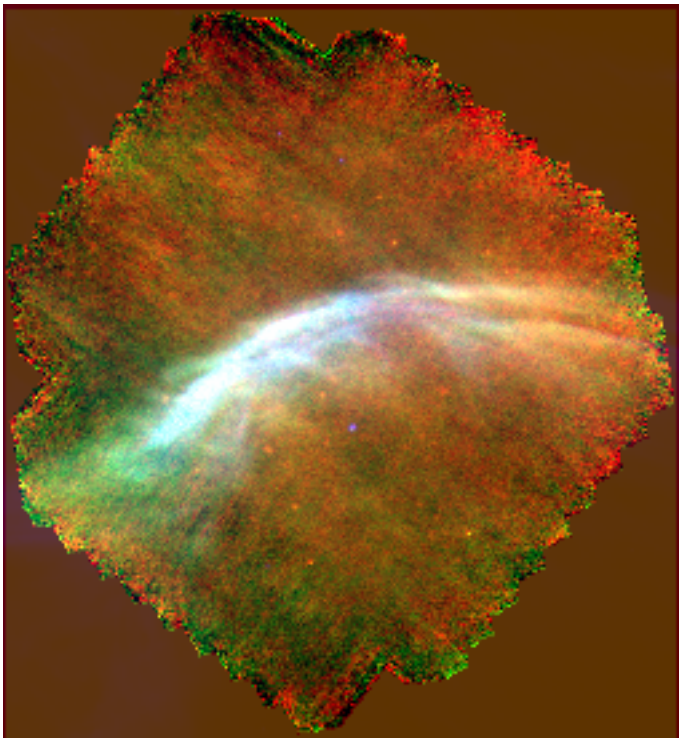

Figure 1.3: A far-infrared view of the bow shock driven by runaway star ζ Oph (spectral class Be) as seen by the Spitzer Space Telescope and Herschel Space Observatory. Blue colour represents 24 , green 70 and red 160 μm light. (Image made by the author from the Spitzer and Herschel data.)

Despite their relatively low brightness, the infrared band also allows the spectroscopic observations of these objects to be performed, which provide important insights into the object + bow shock system, the interstellar matter and the astrophysics of shocks in general. However, these observations are quite rare, as the observing time for the space-based infrared missions is limited by the supply of coolant and other science proposals, thus making any systematical spectroscopic studies not possible. [23], [24], [12]

1.2.2 Optical band

There are only a few unambiguous detections in the optical bands because bow shocks are normally very faint in this spectral region. However, there are a few emission lines (most notably Hα and some emission lines of sulphur, nitrogen and oxygen) that allow the detection of optical bow shock counterparts using narrowband observations. Optical spectroscopy is also possible, but it is challenging because of the low brightness of bow shocks in the optical part of the spectrum. On the other hand, it can be carried out by the ground-based telescopes. [10], [13]

1.2.3 Ultraviolet band

The opacity of the atmosphere and the interstellar gas to the ultraviolet radiation and the engineering challenges make ultraviolet observations very finicky. Several ultraviolet bow shock counterparts have been observed around non-stellar sources but ultraviolet observations of stellar bow shocks are rare. [25], [26], [20]

1.2.4 High energies

Unlike the other astrophysical objects involving shocks (e.g. supernova remnants), the stellar bow shocks have not been of much interest to high-energy astronomy. However, the recently developed theoretical models predict the production of high-energy photons by non-thermal radiative processes in quantities sufficiently large to be detected in X-rays and γ-rays. However, there are very little observational constraints to these phenomena, as only two likely bow shock high-energy counterparts have been detected to this date. The data acquired by the modern high-energy missions such as the European Space Agency's (ESA) X-ray Multi-Mirror Mission (XMM-Newton), the X-ray Astronomy Satellite 'Suzaku', the Chandra X-ray Observatory and the Fermi Gamma-ray Space Telescope may prove to have a lot of untapped potential for the bow shock research. [27], [28], [29], [30]

1.2.5 Radio

There is only one reported detection of radio emission from a stellar bow shock. This emission is most likely of non-thermal origin, probably synchrotron radiation generated by the interaction of relativistic electrons with the magnetic field of the source. [31]

1.3 Motivation

The area of astrophysics studying bow shocks is a rapidly expanding and riveting field of study with a lot of potential for research on all levels.

- The presence of a bow shock may be a secondary attribute of a runaway star or a system. Its presence and properites give us valuable insight into the kinematics of the system, especially when the proper motion measuremements are unreliable or non-existing. This is often the case when surveing high-velocity stars in great distances. Another example is studying X-ray binaries, which frequently do not have, or have only a faint or a disputed optical conterpart.

- The symmetry axis of a bow shock generated by a supersonically moving star reflects the direction of motion of the star with respect to the ambient medium, which also could be in motion relative to the local standard of rest at the location of the star. This means that the star itself does not need to have a high peculiar velocity for a bow shock to form, for example, high velocity outflows emanating from star clusters or associations may create a bow shock around low velocity stars in the cluster/association vicinity. The presence and orientation of bow shocks near these clusters and association can be used to study these outflows.

- The bow shocks of runaway stars with strong stellar winds may serve as particle acceleration sites. The conversion of stellar wind luminosity into particle acceleration power has an efficiency similar to those in supernova remnants. Thus, the runaway bow shock-driving stars can produce a significant fraction of the Galactic cosmic-ray electrons. This is, however, poorly constrained, as the observations are scarce, dedicated bow shock surveys are in their infancy and the physics behind the cosmic ray acceleration needs to be better understood. More theoretical work and observations studying this problem are needed.

- The properties of stellar bow shocks give us valuable insight into stellar mass-loss rates , wind properties and the properties of the surrounding interstellar medium.

Chapter 2

Bow shocks and other bits of relevant astrophysics

In this section I will discuss the relevant astrophysics that will be helpful when interpreting our findings later in the text. The section is started off by a brief discussions on bow shocks themselves and what is currently known about them. I also provide sections containing some relevant topics from different areas of astrophysics that will be useful in interpreting the data in the practical part of this thesis. These include a section on objects that are commonly mistaken for bow shocks and some brief discussion of Strömgren spheres.

2.1 Basic morphology of bow shocks

Stellar wind bow shocks are cometary structures due to the supersonic passage of wind-blowing stars. They sweep up interstellar matter into thin, dense shells, which may be revealed by their postshock emission or by scattered light, and provide a means of studying winds that might otherwise go undetected. Since the existence of bow shocks was revealed only quite recently by the space missions operating in the infrared, our understanding of the physics behind these objects is very limited.

A star moving through a slower interstellar medium will form a thin layer of swept-up gas. An early-type star, that has developed strong stellar winds (for example an OB star) will stack matter on a thicker layer.

If the stellar motion is supersonic with respect to the ambient gas velocity, shock waves are produced. A discontinuity surface is formed, and two shock fronts in opposite directions. A 'forward' shock in the direction of the stellar motion travels with a velocity similar to the stellar velocity. A 'reverse' shock from the discontinuity to the star has a velocity of the order of the stellar wind terminal velocity, which can be, in some cases, a few thousands of $\mathrm{km\,s^{-1}}$. Fig. 2.1 shows a simplified scheme of the situation. The width of the discontinuity will depend on the cooling process: adiabatic, radiative or a mixed case. Ideally, four regions can be identified: the closer to the star with free wind, that of shocked wind, the shocked ambient matter region and the not-yet-disturbed ISM region.

The matter surrounding the stars is piled-up in a feature that resembles the sea foam which is pushed by the bow of a ship, from where the stellar bow shock takes its name. For the faster stars, it resembles a cometary tail. [32]

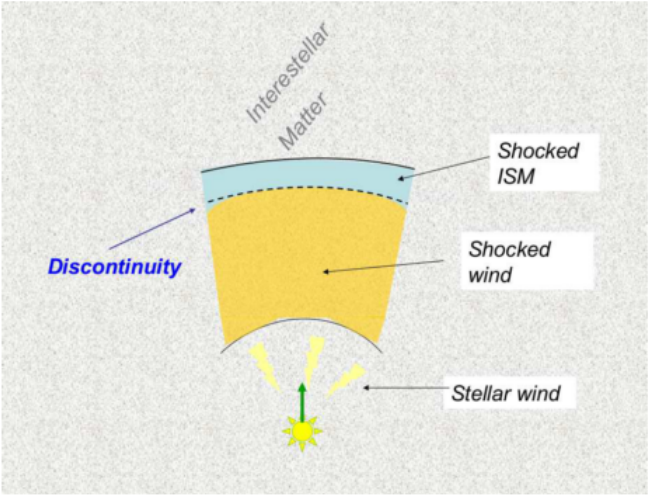

Figure 2.1: Scheme of a stellar bow shock generated by a star with supersonic motion related to the ambient medium.

The theory of momentum-supported bow shocks was first developed by Baranov et al. (1971 [33]), who were motivated by the problem of the interaction of the solar wind with the local interstellar medium. They considered the collision of an isotropic stellar wind with a uniform ambient medium, including the supersonic motion of the star with respect to that medium, and solved numerically for the shape of the bow shock. The exact analytic solution was presented by Wilkin (1996 [34]), who stresses the importance of the conserved momentum within the shell. This leads to simple formulas giving the shell's (arc's) shape, mass column density, and velocity of shocked gas at all points in the shell. I adress the topic in more detail in the section below.

2.1.1 Wilkin's bow shock shape

The stellar wind drives a shock into the ambient medium while the supersonic wind is abruptly decelerated, leading to two layers of shocked gas. These layers are assumed to mix, and postshock cooling is assumed to be so efficient that the dense shell has negligible thickness compared to the distance to the star. The star moves with constant velocity of magnitude $v_\star$ in a uniform medium of density ρ_a. The isotropic stellar wind has mass-loss rate $\dot{M}$ and speed v_∞, yielding a cometary structure with the stellar velocity vector as symmetry axis. The flow is assumed to be hypersonic, so pressure forces are neglected. In this idealized model, the thin shell is fully described by three quantities: the shell's radius $R(\theta)$, mass surface density $\sigma(\theta)$, and the tangential speed $v_t(\theta)$ of shocked material flowing along the shell, where θ is the polar angle from the axis of symmetry, as seen by the star at the coordinate origin.

Let the z-axis be the axis of symmetry of the shell, with the stellar motion in the $\hat{\mathbf{e}}_\mathbf{z}$-direction (toward the right in Fig. 2.2). In the frame of the star, the ambient medium appears as a uniform wind in the $-\hat{\mathbf{e}}_\mathbf{z}$-direction. The stellar wind and the ambient medium collide head-on at $\theta = 0$, and the radius of this starting point of the shell is found by

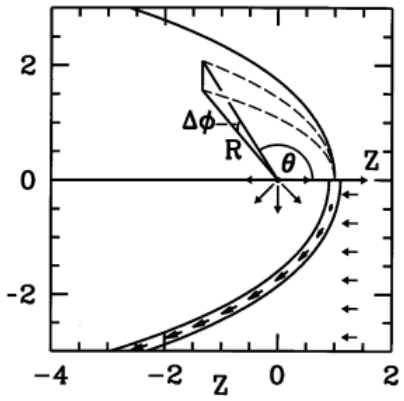

Figure 2.2: Thin-shell bow shock model. The bottom panel shows the wind, ambient, and tangential flows in the frame of the star while the top panel defines the spherical coordinate system with the star at the origin.

balancing the ram pressures of the wind and ambient medium,

$$\rho_w v_\infty^2 = \rho_a v_\star^2, \tag{2.1}$$

which yields

$$R_0 = R_s = \sqrt{\frac{\dot{M} v_\infty}{4\pi \rho_a v_\star^2}}. \tag{2.2}$$

This stand-off distance sets the length scale of the shell. The shape of the shell is a universal function, which is scaled according to equation (2.2) to accomodate all values of the four dimensional parameters ($\dot{M}$, v_∞, ρ_a, $v_\star$).

The fluxes of mass and momentum crossing an annulus of the shell, $2\pi\Phi_m(\theta)$ and $2\pi\Phi_t(\theta)$ are given respectively by

$$\Phi_m = (R\sin\theta)\sigma v_t,\ \Phi_t = (R\sin\theta)\sigma v_t^2. \tag{2.3}$$

In steady state, the mass traversing a ring of the shell at polar angle θ from the stand-off point is precisely that mass flux from the stellar wind intercepted by the solid angle of the forward part of the shell plus the contribution from the ambient medium striking the circular area of the projected cross section of the shell:

$$2\pi\Phi_m = \dot{M}\frac{\Omega}{4\pi} + \pi\varpi^2\rho_a v_\star, \tag{2.4}$$

where $\Omega = 2\pi(1-\cos\theta)$ is the shell solid angle from the axis to the annulus at θ, and the cylindrical radius ϖ is $R\sin\theta$.

Since the calculations leading to the bow shock parameters are quite lengthy, they are not discussed here. However, they can be found in the paper [34]. The calculations yield the prescription for the shells shape:

$$R(\theta) = R_0 \csc\theta\sqrt{3(1-\theta\cot\theta)}. \tag{2.5}$$

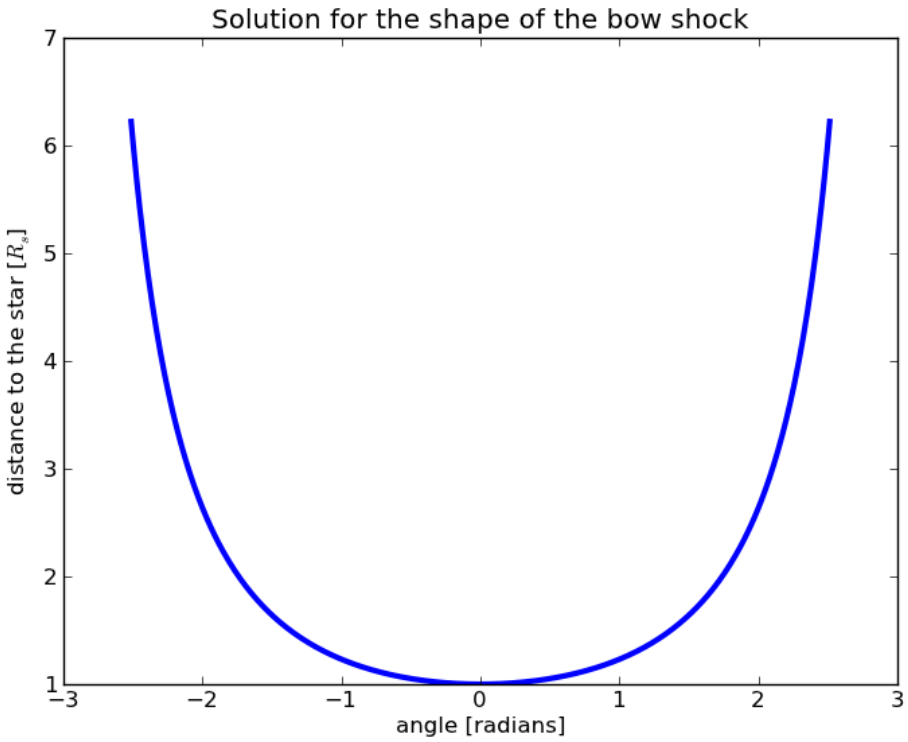

Figure 2.3: The solution for the shape of the bow shock as given by Wilkin (1996 [34]).

The solution is graphed in Fig. 2.3. Transferring the solution into physical units gives us the theoretical bow shock shape (see Fig. 2.4).

Using the previous equation, we have

$$\tilde{\varpi}^2 = 3(1 - \theta \cot\theta). \tag{2.6}$$

Referring to equation (2.3), the tangential velocity in the shell is $v_t = \Phi_t/\Phi_m$, which yields

$$v_t = v_\star \frac{\sqrt{(\theta - \sin\theta\cos\theta)^2 + (\tilde{\varpi}^2 - \sin^2\theta)^2}}{2\alpha(1-\cos\theta) + \tilde{\varpi}^2}, \tag{2.7}$$

where $\alpha = v_\star/v_\infty$ is a nondimensional parameter of the problem. The mass surface density is given by $\sigma = \Phi_m^2/(R\sin\theta)\Phi_t$, which yields

$$\sigma = R_0 \rho a \frac{\left[2\alpha(1-\cos\theta) + \tilde{\varpi}^2\right]^2}{2\tilde{\varpi}\sqrt{(\theta - \sin\theta\cos\theta)^2 + (\tilde{\varpi}^2 - \sin^2\theta)^2}}. \tag{2.8}$$

The tangential velocity and mass surface density are plotted in Fig. 2.5 for several values of α. [34]

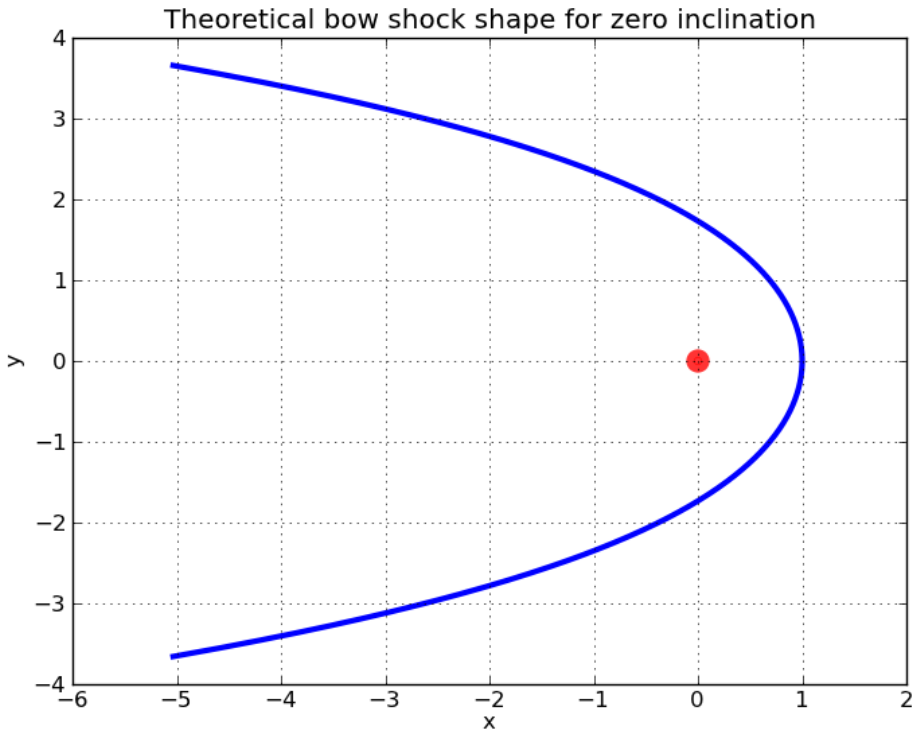

Figure 2.4: A theoretical bow shock (zero inclination) according to the model by Wilkin(1996 [34]). The star driving the shock is placed in the origin and the axes are in arbitrary units. The stand-off distance is chosen to be 1.0.

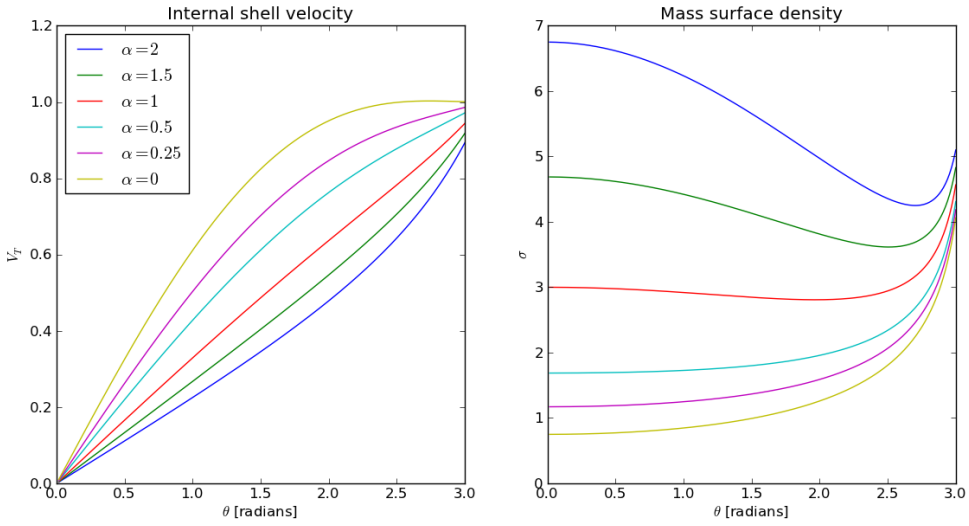

Figure 2.5: Internal shell velocity in units of $v_\star$ (left) and mass surface density in units of $R_0\rho_a$ (right) according to the model by Wilkin(1996). The mass per unit area σ is defined for a line of sight that is normal to the shell.

2.2 Particle acceleration and radiation processes

Bowshocks from runaway stars produce thermal emission by radiative heating of the swept-up dust by the stellar radiation field. The infrared signal of the heated dusty bowshock is strongest in the far infrared. The dust temperature can be understood in terms of dust models. For a typical bowshock of a runaway star, a fraction $\sim 10^{-2}$ of the star bolometric luminosity is emitted in the infrared. The shocked ISM can also produce thermal emission through free-free interactions (Bremsstrahlung).

Relativistic particles can be accelerated at strong shocks producing non-thermal emission. Benaglia et al. (2010 [31]) have reported non-thermal radio emission from the bowshock of the runaway star BD $+43^{\circ}3654$. This emission is thought to be synchrotron radiation generated by the interaction of relativistic electrons with the magnetic field of the source. Lopez-Santiago et al. (2012 [28]) have detected X-ray emission from the bow shock produced by the runaway star AE Aur (see Fig 2.6). This emission is produced mainly by inverse Compton up-scattering of infrared photons from dust in the shock front.

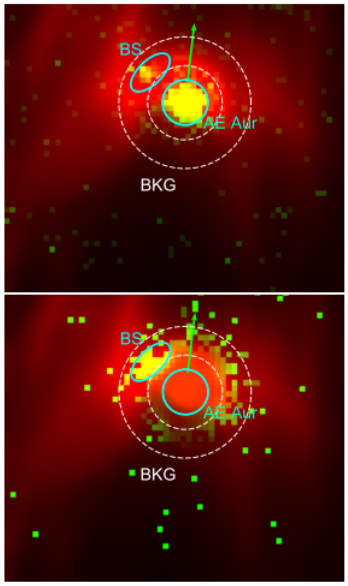

Figure 2.6: Top: WISE 12 μm image (red) and EPIC (XMM-Newton) pn count image of AE Aur in the 1 – 8keV band (green). Bottom: same as top panel with pn median photon map in the 0.3 – 8 keV in green. The bow shock emission is marked by the elliptical region.

Shocks transfer kinetic energy to non-thermal particles through particle acceleration. The acceleration mechanism is diffusive shock acceleration, the so-called Fermi I mechanism. In this mechanism particles are accelerated by successive bouncing across the shock, gaining energy in each cross. The particle deflection is mediated by magnetic field irregularities. These irregularities are expected from turbulent and magnetic instabilities. For the mechanism to operate, it is necessary that the particles in the shocked medium (downstream) can effectively diffuse and reach the shock.

The particle energy gain in each cycle (upstream-downstream-upstream) is

$$\Delta E/E \propto (v_s/c), \tag{2.9}$$

where v_s is the shock velocity. After k cycles the particle energy is

$$E = E_i\left(1+\frac{\Delta E}{E}\right)^k, \tag{2.10}$$

where E_i is the initial energy. The time that a particle requires to accelerate up to an energy E is given by

$$t_{acc} = \eta\frac{E}{eBc}. \tag{2.11}$$

Here, B is the magnetic field in the acceleration region, and η is the acceleration efficiency:

$$\eta \sim \frac{1}{10}\frac{r_g c}{D}\left(\frac{v_s}{c}\right)^2, \tag{2.12}$$

where D is the diffusion coefficient, and $r_g = E/(eB)$ is the particle gyroradius. Fast shocks are more efficient accelerators than slow shocks. The resulting spectrum of injected particles by this mechanism is a power-law, i.e.$Q(E) \propto E^{-\alpha}$, with $\alpha \sim 2-2.2$.

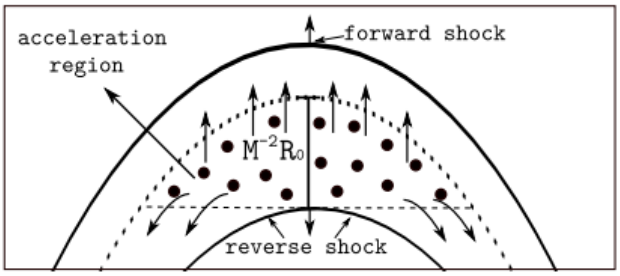

Figure 2.7: Scheme of the system of shocks (not to scale). The acceleration region is indicated by dots.

Fig. 2.7 shows a system of two shocks within the bow shock. Let us consider an initial supra-thermal (highly energetic) population of relativistic particles, electrons and protons, which are accelerated in the adiabatic shock (reverse shock). This shock is faster than the forward shock, so in the reverse shock the relativistic particles are accelerated more efficiently by the Fermi mechanism. All equations given above are valid for planar shocks. The width of the shocked stellar wind, Δ, can be estimated as $\Delta \sim M^{-2}R_0$, where M is the Mach number of the shocked wind. The acceleration region is assumed as a small region near the bowshock apex, of scale length $\sim \Delta$. [29]

The available power in the system is the kinetic power from the stellar wind:

$$L_T \sim \frac{1}{2}\dot{M}v_\infty^2. \tag{2.13}$$

The kinetic power available in the acceleration region is $L = fL_T$, where f is the ratio of the volume of a sphere of radius R_0 and the volume of the acceleration region. A small fraction of this kinetic power goes into relativistic particles ($L_{rel} = q_{rel}L$). Del Valle & Romero (2012 [29]) adopt a standard fraction $q_{rel} = 0.1$.

The electrons lose energy mainly by inverse Compton (IC) scattering, synchrotron radiation, and relativistic Bremsstrahlung. Protons lose energy through proton-proton

inelastic collisions with the shocked wind material. These interactions produce neutral and charged pions; the former decay and produce gamma rays. The latter decay into secondary electrons/positrons and neutrinos.[29]

Del Valle & Romero (2012 [29]) investigate the losses for an O4I star and an O9I star. They determine that in the O4I star system the IC scattering of IR photons dominates the radiative losses. For the O9I star, the IC scattering of IR photons and synchrotron radiation prevail among the radiative losses.

They also construct a non-thermal radiative model of ζ Oph and predict that the bow shock produces a significant amount of γ radiation that should be detectable by The Fermi Gamma-ray Space Telescope. However, Schulz et al. (2014 [35]) detect no emission from ζ Oph in the Fermi energy range and challenge the model. So the problem of particle acceleration and non-thermal processes in stellar bow shocks is still very much unresolved. More observational constraints and modelling work needs to be done in this field.

2.3 Objects with similar morphologies

A large number of astrophysical processes may give rise to arcuate structures in the ISM. Thus it is not surprising that they are ubiquitous especially in the optical and infrared images of the sky. The vast majority of these objects are not, of course, stellar bow shocks. A very simple condition that holds true for all stellar bow shocks can be used to tell them apart from most of other arcuate structures. A bow shock needs to have a star or a stellar system laying on its axis of symmetry. However, there are still several types of objects that satisfy this condition and are not bow shocks. These objects can be (and most likely are) sometimes misclassified as genuine stellar bow shocks. Fortunately, multiwavelength observations of their surroundings, photometry or spectroscopy of their putative driving stars and peculiar proper motion measurements can be used to distinguish them from stellar bow shocks.

2.3.1 Dust waves and bow waves

Dust waves and bow waves are types of structures most easily mistaken for stellar bow shocks. So far only a few of these kind of objects have been identified and studied up close. It is very likely that a significant number of catalogued bow shocks are actually dust or bow waves.

The astrophysics of bow waves and dust waves is a subject of ongoing research but their existence has already been proposed by Buren & McCray [23] as early as 1988. This area of research has then been neglected until only recently. In early 2014, Ochsendorf et al. released two papers addressing these phenomena. In their earlier paper [36] they reveal a prominent arc-shaped structure around star σ Ori AB which is very reminiscent of a stellar bow shock (see Fig. 2.8) . However, this star is thought to display the weak-wind phenomenon and the large separation between the apex of the extended arcuate emission and the star is too large to be explained using the bow shock interpretation, since its stellar wind is too weak to produce a bow shock having this kind of stand-off distance. Instead they come up with an alternate explanation. They attribute this dust structure to the interaction of radiation pressure from the star with dust carried along by the IC 434 photo-evaporative

flow of ionized gas from the dark cloud L1630. Large scale flows of ISM and so-called champagne flows (rapidly expanding flows of ionized gas from a high density clouds into surrounding tenuous ISM) may interact with a star, when radiation pressure stalls dust, piling it up at a significant distance and force it to flow around the star, creating an arc of extended mid-infrared emission. The classical stellar wind bow shock thus cannot form, because its theoretical stand-off distance is well within the bow (dust) wave and the ISM has already been diverted by the radiation pressure. The difference between the dust wave and bow wave is that a dust wave forms when the dust is stopped by the radiation pressure and decouples from the gas, while in a bow wave the dust and gas stay coupled. It is thought that for higher densities of the flow, the coupling is more efficient and a bow wave will form, containing both dust and gas. While these structures are very interesting in their own right, the detailed discussion of their astrophysics is not the subject of this work. One should refer to Ochsendorf et al. (2014a [36]) for a more detailed insight into this topic.

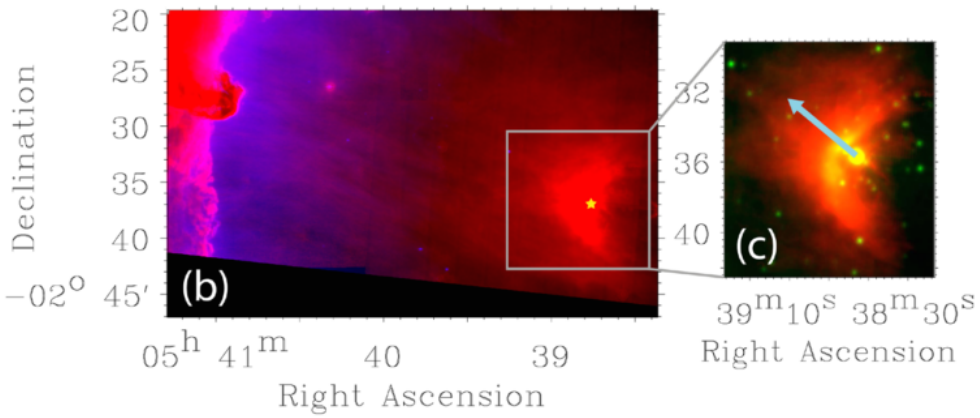

Figure 2.8: The dust wave around σ Ori AB. The left image shows the neighborhood of the system. Blue represents Hα emission, whereas red is MIPS 24μm emission. The well-known Horsehead nebula is visible at the top left. The right image represents the close enviroment of σ Ori AB. The proper motion of the star vector is overplotted on the image. Green is light WISE 12 μm channel, while red corresponds to MIPS 24μm light.

Dust waves and bow waves may also form in bursting interstellar bubbles. These bubbles are a very common feature of the mid-infrared sky. Assisted by volunteers from the general public, about 5000 bubbles have now been identified in the Galactic plane. However, the physics giving rise to these objects is still being debated. Traditionally, the formation of bubbles is explained through the input of a powerful stellar wind, even though the direct evidence supporting this scenario is lacking. Ochsendorf et al. (2014b [37]) propose, that at least some bubbles, especially those blown by stars with $\log(L/L_{sun}) < 5.2$, are formed by thermal pressure of the gas accompanying ionization instead of a stellar wind.

Fig. 2.10 describes the formation of a bow wave (dust wave) inside an interstellar bubble. (A) The bubble is created as the overpressure of the hot, ionized interior (yellow) causes the bubble to expand inside the natal cloud, sweeping up neutral gas in a dense shell (blue). If the expansion is supersonic, a shock forms on the neutral side of the shell (dashed line). (B) If the ionized gas contains a density gradient and/or the bubble is puctured (by reaching the boundary of the cloud or by an outside stimulus), a flow

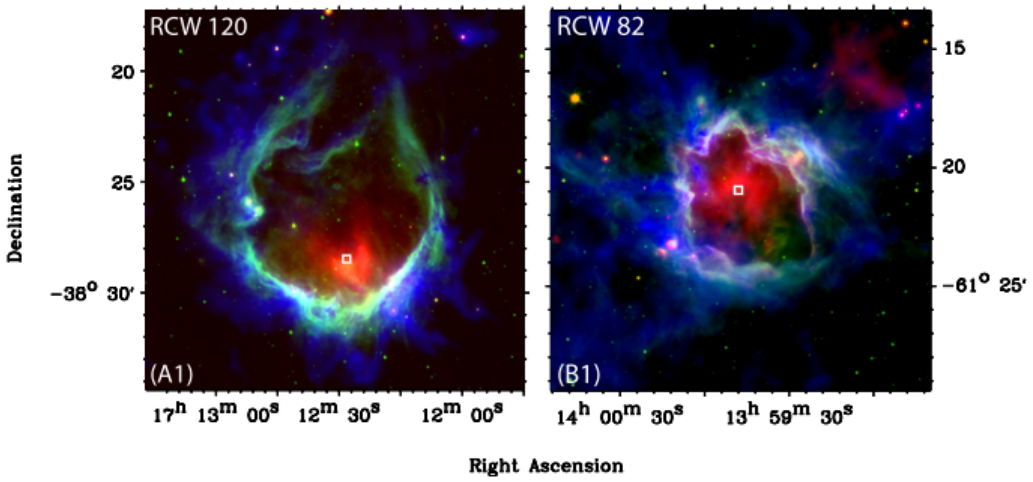

Figure 2.9: The infrared view of the HII bubble RCW 120 and RCW 82. The green colour (IRAC 8μm) traces Polycyclic aromatic hydrocarbon (PAH) emission from the inner edges of the bubble. The red light (MIPS 24 μm) traces emission from dust grains from an arcuate structure formed near the central ionizing source of the bubble (marked by a white square). Blue (SPIRE 250μm) is the emission from dense cold dust surrounding the bubble.

of ionized gas will stream towards lower density and ultimately into surrounding ISM, relieving the bubble from its pressure. (C) Dust is dragged along in ionized flow, where upstream dust approaching the ionizing source (star) will be heated and halted by radiation pressure, resulting in a bow wave or a dust wave, depending on how the gas and dust are coupled together. Dust waves and bow waves can then be traced at mid-IR wavelengths. The escaping gas will eventually be replaced by a flow of ionized gas evaporating from the inner wall of the swept-up shell.

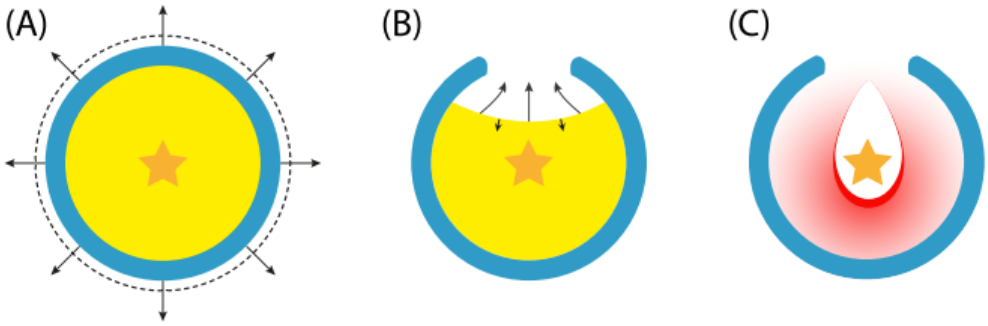

Figure 2.10: A scheme showing the formation of a dust wave (bow wave) inside an interstellar bubble.

It has been shown that a dust wave (bow wave), where radiation pressure acts on the surrounding medium, differs fundamentally from a classical bow shock, where the ram pressure of the star and ISM balance. According to our previous definition, a dust wave increases the number density of dust and will therefore solely emit in mid-IR wavelengths with respect to the background emission, whereas a bow shock will shock both gas and dust

and it is therefore possible to detect a bow shock in gas emission lines as well as in mid-IR wavelengths. Indeed, spectral observations using Spitzer have revealed several prominent infrared gas emission lines in some bow shocks (e.g. Vela X-1) [38]. However, only a very limited number of bow shocks and bow shock candidates have been investigated using spectroscopy, so this method cannot be utilized on a large scale. It is also now impossible to make any more spectral observations in the infrared, as Spitzer has run out of coolant and is no longer capable of spectroscopy and there is currently no other mission capable of similar observations. Optical narrow-band imaging (e.g. in Hα filter) and spectroscopy have also been conducted with some success [10], but there are several drawbacks associated with these methods. The bow shock emission is often very faint when it is compared to the driving star and the absorption in the Galactic plane (the most bow shocks are driven by early-type massive stars, so they never get too far from the Galactic plane because of their limited lifetime) also limits the usability of observations in the optical bands so only relatively close bow shocks can be observed.

It is also possible to check for a discrepancy between the observed stand-off radius of a bow shock candidate and the stand-off radius that can be calculated if the distance, stellar wind parameters, velocity of the star and density of the ISM are known. However, some of these parameters are difficult to reliably determine for this method to be usable.

An investigation of wider environs around a bow shock candidate may also yield some insight. It is possible to check whether the bow shock candidate lies inside the interstellar bubble. Also checking for the objects that may be sources of large-scale flows and then comparing the axis of symmetry of the arc to the direction of the tentative flow may also be useful.

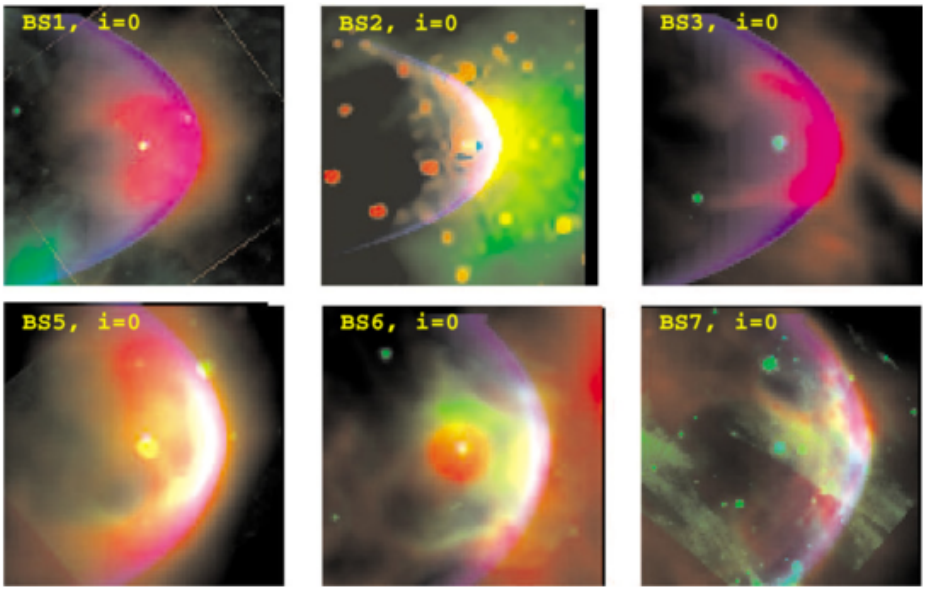

Figure 2.11: Images of selected possible bow shocks studied by Kobulnicky et al. with MIPS 24 μm in red, IRAC 8 μm in green and a simulated bow shock, based on the analytical shape parametrization of Wilkin, in blue.

Despite the known limitations of Wilkin's bow shock analytical shape parametrization,

this method has been used to differentiate between the stellar wind bow shocks and other types of objects with similar morphologies. For example, Kobulnicky et al. (2010 [39]) construct synthetic bow shocks according to Wilkin's parametrization and overlay them on their images. The arcs that correspond well to the analytical bow shocks are then confirmed as genuine stellar bow shocks. Using this method, objects BS2, BS5 and BS7 in Fig. 2.11 are classified as bow shocks. It is unknown how well this method can be used to differentiate between bow shock and dust waves (bow waves). This problem will be investigated later in the practical part of this thesis. It can be concluded that for the stars that may be susceptible to the weak wind problem, a lot of caution is required when interpreting mid-infrared arcs that may be associated with them.

2.3.2 Young stellar objects and star-forming regions

Young stellar objects (YSOs) within regions with a lot of star formation can also produce morphologies reminiscent of stellar wind bow shocks. Most notably, massive star formation triggered in the heads of gas columns being eroded from the outside (for example by combined winds emanating from an OB association or open cluster) may produce arcuate infrared morphologies, especially in the more evolved stages. A pre-main sequence object within the disintegrating pillar can illuminate a rim of material which can be similar to a bow shock. Infrared photometry can be used to distinguish these YSOs from standard stars, as YSOs produce SEDs that rise towards longer wavelengths. [39]

2.4 Strömgren spheres

Strömgren spheres are spheres of ionized hydrogen (H II) around a young star of the early spectral classes. In this section I describe how these objects form and provide the background needed later in this work.

Considering atoms of a given species we designate their discrete energy levels by index j, and the ensemble of continuous levels resulting from the ionisation by index k (obviously levels of higher energy than the j levels). In the presence of ionizing radiation, let us call P_{jk} the probability of photoionization per second from level j, and n_j the population of level j. n_k is the population of level k and P_{kj} the probability of recombination with a free electron to level j. Assuming ionization equilibrium, we can write

$$n_k \sum_j P_{kj} = \sum_j n_j P_{jk}. \tag{2.14}$$

Letting σ_j be the cross-section for capture of an electron to level j, we have

$$P_{kj} = n_e \langle v \sigma_j \rangle = n_e a_j, \tag{2.15}$$

where n_e is the density of free electrons and v their mean velocity. We assume a maxwellian distribution of electron velocities with a temperature T_e.

Similarly, if $s_j(\nu)$ is the photoionization cross-section from level j by photons with frequency ν, $n_{phot}(\nu) = u_\nu / h\nu$ being the density of these photons (u_ν is the radiation energy density), then

$$P_{jk} = \int_{\nu} c n_{phot}(\nu) s_j(\nu) d\nu = b_j. \tag{2.16}$$

We can now write the ionization equilibrium equation for the two consecutive ionic states of the considered element, with ionizations r and r + 1:

$$n_{r+1} n_e \sum_j a_j = \sum_j n_{r,j} b_j. \tag{2.17}$$

Radiative cascades from levels j to the fundamental level of the atom or ion being generally very fast, of the order of a few 10^{-9} second, and collisional excitations from the fundamental to excited j levels being generally negligible, we can consider that ionizations are only from the fundamental level, so that

$$n_{r+1} n_e \sum_j a_j \simeq n_r b_1. \tag{2.18}$$

In the case of hydrogen there is a further simplification: because hydrogen supplies most of free electrons, $n_e \simeq n_i$, n_i being the density of the hydrogen ions. If n_0 is the density of hydrogen atoms and x its degree of ionization,

$$n_H = n_0 + n_i, \tag{2.19}$$

$$x = n_i/n_H = n_e/n_H, \tag{2.20}$$

$$a = \sum_j a_j, \tag{2.21}$$

the equation of ionization equilibrium is then

$$x^2 n_H^2 a = (1-x) n_H b_1, \tag{2.22}$$

hence

$$\frac{1-x}{x^2} = \frac{n_H a}{b_1}. \tag{2.23}$$

Let us now consider a hydrogen cloud with uniform density n_H surrounding an ionizing star at the centre. The absorption coefficient of hydrogen in the Lyman continuum is

$$\kappa_\nu = s(\nu) n_0 = 6.6 \times 10^{-18} (\nu_1/\nu)^3 n_0, \tag{2.24}$$

ν_1 being the frequency of the Lyman discontinuity ($\nu_1 = 3.288 \times 10^{15}$ Hz).

At a distance r from the star, the optical depth in the Lyman continuum is, neglecting absorption by dust

$$\tau_\nu = \int \kappa_\nu d\nu = 6.6 \times 10^{-18} (\nu_1/\nu)^3 \int_0^r n_0 dr. \tag{2.25}$$

The absorption is very abrupt if the hydrogen is not totally ionized, except where the density is extremely small. We can see that the ionization is almost complete out to a radius R_{st}, beyond which there are no ionizing photons, those inside this radius being absorbed by the few neutral atoms resulting from recombinations.The gas is neutral outside this radius

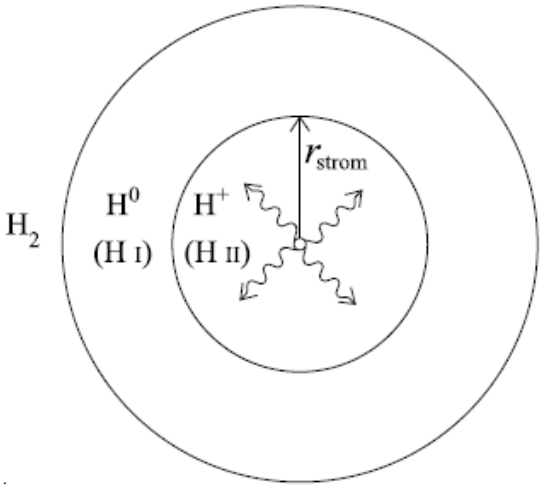

Figure 2.12: Schematic illustration of the Strömgren of ionized hydrogen that is produced around a hot star via photoionization. Inside the radius r_{strom} (R_{st} in the text), the hydrogen is almost completely ionized, i.e., there is an H II region. Beyond this radius, the hydrogen is neutral, since all photons capable of ionizing it have been absorbed.

and ionized inside, forming the Strömgren sphere. Let us now calculate the radius R_{st} for the total density n_H and the ionizing flux $S(0)$ emitted by the star over 4π steradians. The ionizing flux $S(R_{st})$ drops to zero at the surface of the Strömgren sphere. The number of ionizations per second and per cm^3 is from (2.22)

$$(1-x)n_H b_1 = x^2 n_H^2 a \simeq n_H^2 a, \tag{2.26}$$

since hydrogen is almost totally ionized in the H II region ($x \simeq 1$).

We have to take into account the fact that any recombination to the fundamental level yields a photon which will ionize the next neutral atom. Such recombinations must not be accounted for. Only recombinations to higher levels ($j \geq 2$) need be considered, and the recombination coefficient a must then be replaced by

$$a^{(2)} = \sum_{j>1} a_{kj} = 1.627 \times 10^{-13} T^{-1/2} (1 - 1.657 \log T_4 + 0.584 T_4^{1/3}) \text{cm}^3\,\text{s}^{-1}, \tag{2.27}$$

with $T_4 = T/10^4$K.

The radius R_{st} is such that the number of recombinations inside the volume is equal to the number of ionizations, so that

$$R_{st} = \left[\frac{3S(0)}{4\pi n_H^2 a^{(2)}} \right]^{1/3} \tag{2.28}$$

The preceding description is very idealistic. It is rare to find an isolated, spherical H II region with a true ionization structure. In fact the ionized medium has generally an heterogeneous structure. Moreover, massive stars tend to form near the surface of molecular clouds, so that the HII region tends rapidly to pierce the cloud and to expand outside it due to its high pressure. [40], [41]

Chapter 3

Data acquisition and reduction

This thesis is mostly experimental and is based on the infrared and high-energy observational data obtained by space missions, as the ground-based instrumentation cannot be used to observe in these bands. Despite the fact that there is a lot of reduced science-grade data available in the archive which may be sufficient for a lot of purposes, the quality of these data products is often not sufficient for studying faint, extended objects with a fine structure that are stellar bow shocks. Thus, a significant number of observations had to be re-reduced for them to be sufficient for my analysis. For this reason, the topic of data reduction plays a pivotal role throughout this thesis. In this section, I describe the capabilities of the instruments and missions that were utilized and the processing steps necessary to obtain science-grade data used in this work.

3.1 Spitzer Space telescope

The Spitzer Space Telescope is the last of the NASA Great Observatories program, covering the spectral regions from mid to far infrared. Spitzer carries three instruments onboard: IRAC (Infrared Array Camera)[42], IRS (Infrared Spectrograph)[43] and MIPS (Multiband Imaging Photometer for Spitzer)[44], but after the depletion of the liquid helium coolant supply only IRAC remains functional with limited capabilities. [45]

Infrared Array Camera (IRAC) provides $5.22'$x$5.22'$ images at 3.6, 4.5, 5.8 and 8 μm. All four detector arrays in the camera are 256x256 pixels in size, with a pixel size approximately $1.2''$x$1.2''$. The first two short wavelength channels use In:Sb detector arrays while the other two channels use Si:As detectors. For more information one can refer to Table 3.1 or IRAC Instrument Handbook [46].

The Multiband Imaging Photometer for Spitzer (MIPS) was capable of imaging and photometry in broad spectral bands centered nominally at 24, 70, and 160 μm, and of low-resolution spectroscopy between 55 and 95 μm. The instrument contains three separate detector arrays (128x128 pixel Si:As, 32x32 pixel Ge:Ga, 2x20 stressed Ge:Ga), providing high-sensitivity, low-noise and diffraction-limited performance. In this work, we use the data only from the short-wavelength 24 μm detector giving a bandpass from 20.8 to 26.1 μm with a weighted average wavelength of 23.68 μm, having approximately $5'$ field of view (FOV) and the point spread function (PSF) size of $6''$ full width at half maximum. For more information one may refer to MIPS Instrument Handbook[47].

The reduced (level 2 - pbcd) data that can be obtained via Spitzer Heritage Archive are often of sufficient quality to be used for some scientific purposes. However, these products exhibit numerous artifacts (streaks, bars, etc.) which make them unsuitable for my analysis. Thus, a custom reduction of level 1 (basic calibrated products - bcd) became necessary. Nevertheless, a quick inspection of the pbcd data was still helpful when choosing a suitable reduction procedure. The reduction of IRAC and MIPS data can be sometimes a bit finicky. I used the Spitzer data (in part) in my Bachelor thesis. A brief and very general description of Spitzer data, MOPEX (MOsaicking and Point source EXtraction), and reduction processes aplicable to the data can be found there [38]. However, for a more serious and throughout discourse, one should consult the MOPEX User's Guide [48] and Spitzer Data Processing Cookbook[49].

Figure 3.1: Left: Spitzer Space telescope. Right: Herschel Space Observatory (Courtesy of NASA, ESO).

3.2 Wide-field Infrared Survey Explorer (WISE)

Operational from December 2009 until the depletion of its coolant in February 2011, the Wide-field Infrared Survey Explorer (WISE) was NASA's infrared mission. Its main scientific goal was to conduct an all-sky mid-infrared survey with a much higher sensitivity than the previous infrared survey missions. WISE is capable of achieving 5σ point source sensitivities better than 0.08, 0.11, 1, and 6 mJy in unconfused regions on the ecliptic

in bands centered at wavelengths of 3.4, 4.6, 12, and 22 μm. Sensitivity improves toward the ecliptic poles due to denser coverage and lower zodiacal background. The angular resolution is 6.1, 6.4, 6.5, and 12.0 arcsec at 3.4, 4.6, 12, and 22 μm, and the astrometric precision for high signal-to-noise sources is better than 0.15 arcsec. WISE vastly outperforms its predecessors. For instance, WISE is achieving a sensitivity more than 100 times better than IRAS in the 12 μm band.

WISE science data processing, archiving, and distribution are performed by the IPAC, California Institute of Technology. The processing software and operations system is based on algorithms, pipelines, and architecture used for 2MASS, the Spitzer Space Telescope, and GALEX projects. Processed WISE images and extracted source data and metadata are be archived and served to the community via the Web-based and machine-friendly interfaces of the NASA/IPAC Infrared Science Archive (IRSA). These products seem to be of sufficient quality for my purposes, so no reprocessing was deemed necessary. [50]

Survey	Band	λ	$\Delta\lambda$
		(μm)	(μm)
Spitzer IRAC 1	3.6 μm	3.53	0.37
Spitzer IRAC 2	4.5 μm	4.47	0.50
Spitzer IRAC 3	5.8 μm	5.68	0.693
Spitzer IRAC 4	8.0 μm	7.75	1.409
Spitzer MIPS 1	24 μm	23.68	5.3
WISE	W1	3.38	0.34
WISE	W2	4.63	0.525
WISE	W3	12.33	3.228
WISE	W4	22.25	1.973
Herschel PACS	blue	70	
Herschel PACS	green	100	
Herschel PACS	red	160	

Table 3.1: Infrared bands and surveys used in this study.

3.3 Herschel Space Observatory

The Herschel Space Observatory (or Herschel, for short) is the largest astronomical telescope ever launched into space. Operated by the European Space Agency (ESA), it was active from 2009 to 2013 and carried a single 3.5-meter mirror and instruments sensitive to the far infrared and submillimetre wavebands. The mission builds upon the legacy of ESA's Infrared Space Observatory and subsequent infrared missions such as NASA's Spitzer and JAXA's Akari, but it also bridges the gap in the spectrum between what can be observed from the ground and the earlier infrared space missions. [51]

The observatory utilized three detectors: PACS, SPIRE and HIFI. The first of them is the Photoconductor Array Camera and Spectrometer (PACS), which was a photometer and medium resolution spectrometer. It had two bolometer arrays for imaging photometry, and two stressed/unstressed germanium galium bolometer arrays for imaging line spectroscopy.

In photometry mode, PACS was capable of simultaneous imaging in 130-210 μm band (red) and in either the 60-90 (blue) or 90-130 μm (green). The camera contained two bolometer detector arrays with 64×32 pixels (blue array) and 32×16 (red array), respectively, providing an instantaneous field-of-view of $3.5 \times 1.75\,\mathrm{arcmin}^2$. PACS' spectrometer used reflection grating and was capable of spectroscopy in 55 to 210 μm. [52]

The Spectral and Photometric Imaging Receiver (SPIRE) consisted of a three-band imaging photometer and an imaging Fourier Transfer Spectrometer (FTS). The photometer carried out broad-band photometry ($\lambda/\Delta\lambda \approx 3$) in three spectral bands centered on approximately 250, 350 and 500 μm, and the FTS used two overlapping bands to cover 194-671 μm (447-1550 GHz). In this work, I only make a limited use of the data obtained by this instrument. [53]

HIFI was the Heterodyne Instrument for the Far Infrared. It was designed to provide spectroscopy at high to very high resolution over a frequency range of approximately 480-1250 and 1410-1910 GHz (625-240 and 213-157 μm). The HIFI data are not used in this work. [54]

All Herschel data used in this work were accessed from the Herschel Science Archive via the Herschel Interactive Processing Environment (HIPE, [55]). In addition to this, HIPE enables user to perform data reduction to science-grade products, visualize the data, perform science analysis and access the Herschel documentation and cookbooks. The Herschel Science Archive also enables us to download already reduced science-grade products, processed through the standard pipelines. All observations are regularly reprocessed in bulk, whenever there is a new release of the Herschel Common Software System (HCSS). As of writing this thesis (late 2014), all products in the Herschel Science Archive have been reprocessed with HCSS 12.1. These products are then used in this work. The highlights of this version include much-improved PACS photometry images for extended emission, produced with both the JScanam and MADMap mapmakers. This work makes use of MADMap products, preserving the morphology and fluxes of the extended emission. The inspection of the HCSS 12.1-processed data covering the objects of interest revealed no apparent need to reprocess the data.

3.4 Chandra X-ray Observatory

The Chandra X-ray Observatory (or Chandra, for short), formerly known as the Advanced X-ray Astrophysics Facility is one of NASA's Great Observatories launched in 1999. Despite its age it is still operational. Its exquisite X-ray imaging capabilities are a great leap forwards when compared to its predecessors, Einstein and ROSAT X-ray missions. Nearly a 100-fold improvement in the imaging capability enables Chandra to study fine structures such as jets and outflows in quasars and active galaxies which had previously been considered 'point' sources, to reveal structure and interactions within clusters of galaxies for which the distribution of hot gas had previously been considered smooth and symmetric, and to allow point source detection to fluxes 100 times fainter due to the reduction of the detector area which accumulates background.

3.4.1 Observational capabilities

Chandra boasts large telescope area, access to the entire sky with more than 85% of it available at any time, high observing efficiency and a long operational lifetime enabling investigations using long time baselines. It houses instruments that could provide imaging and spectroscopy (a low energy transmission grating (LETG, 0.07 to 2 keV range) and high energy transmission grating (HETG, for energies up to 10 keV)), including spatially resolved spectroscopy with at least modest ($E/\Delta E = 10-50$) energy resolution and the ability to locate the measured photons on the sky.

Only one of two different imaging instruments can be moved into the telescope aimpoint at any time. The High Resolution Camera (HRC) employs micro-channel plates similar to the ROSAT and Einstein high resolution imagers. The HRC provides a useful angular resolution of about 0.5 arcsec of the sky but it does not provide a very accurate determination of the X-ray energy. However, when combined with the transmission gratings, particularly the low energy grating, it can achieve an energy resolution of about $E/\Delta E = 1000$. Another advantage of the HRC is that it provides 16 microsecond time resolution for the X-ray events for sources that are positioned on the central micro-channel plate of the spectroscopy array and are below the telemetry saturation level. Because none of the objects that are investigated in this work is covered by the HRC data, I will refrain from the further discussion of this instrument.

The AXAF CCD Imaging Spectrometer (ACIS) employs CCDs as the basic detecting element. It convert X-rays into a number of electrons directly proportional to the photon energy, and clocks these out in a fixed pattern which indicates the position at which the X-ray was imaged. ACIS can detect energies down to about 0.4 keV with a narrow energy window at 0.25 keV. The upper energy cut-off is at around 8 keV. The energy resolution of the CCD varies from about 100 eV at 1 keV to about 160 eV at 6 keV. Similarly to the HRC, the ACIS can be used on its own or in conjunction with one of the observatory's two transmission gratings. [56], [57], [58]

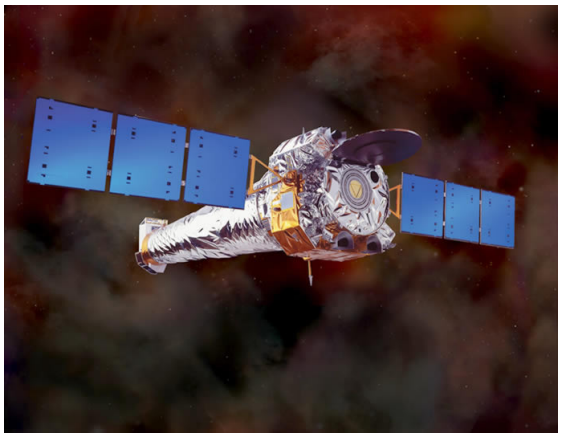

Figure 3.2: The Chandra X-ray Observatory (Courtesy of NASA, ESO).

3.4.2 Obtaining the data, data structure and data preparation

In this work I will heavily rely on the CIAO (Chandra Interactive Analysis of Observations) software package which was first released in 1999 following the launch of the Chandra X-ray Observatory. It is mainly used to analyze Chandra data but it can handle the data from other telescopes as well.[59]

To find out whether my objects of interest have available Chandra data associated with them I made use of WebChaSeR [60] service. WebChaSeR is the web interface to the Chandra Data Archive. It allows users to browse the observation catalog with a variety of search criteria, to display preview images, and to download the data tarfiles. The analysis of the Chandra data requires a lot of computational power, so the usage a conventional personal computer for this task is cumbersome. Thus, most of the analysis was done remotely on more powerful machines and WebChaSeR was used merely to compile a list of observations to download. The desired observations were then downloaded via the CIAO tool *download_chandra_obsid*, that will download the data for the given Chandra Observation Id (ObsId) from the public archive. The files are then stored in the current working directory, using the Observation Id as a directory name. For instance, the data for ObsId 428 would be placed in the directory 428/. Within this directory the files are placed as they are in the archive, namely a top-level directory containing the oif.fits and V&V report, with the remaining data in the primary/ and secondary/ sub-directories.[61], [62]

V&V report stands for 'verification and validation' report and is distributed in PDF format with the data files. It is concerned with any possible exposure losses or other abnormalities that may affect the observation. The observation index file (oif.fits) contains a summary of the data products associated with an observation. It is equivalent to a structured directory listing with descriptive information about the observation. The primary/ and secondary/ subdirectories contain data products necessary for analysis and reprocessing the data. The complete listing of these files can be found in the CXO documentation or in the Introduction to the Data Products thread [63]. Perhaps the most important one is the level 2 event file (evt2.fits) found in the primary directory. This type of data product is common to the X-ray astronomy.

All X-ray detectors measure individual photons. This is in contrast to many instruments for longer wavelengths, which measure integrated flux. The reason for this difference is that X-ray photons have relatively large energies, so single ones can be easily be detected, but have relatively low fluxes, so they are easy to count. The basic data structure is thus a list of detected events, each of which has a set of attributes. Current X-ray instrumentation typically measures the position of the X-ray arrived on the detector, time of arrival, and some attribute which relates to the energy of the photon. In addition to these basic attributes, most event lists also include other quantities which can be used to discriminate good events from background. [63], [56]

It is recommended that all users reprocess their data in CIAO to ensure that the newest software and consistent calibration updates are applied to the dataset before you starting the analysis. This can be done manually using step described in the CIAO science thread on reprocessing [64]. Another option is to use the *chandra_repro* script to reprocess your data and be confident it has the newest calibration applied. The script reads data from the primary/ and secondary/ subdirectories and creates new data products, particularly a new level=2 event file. A new subdirectory repro/, containing these new data products, will be

created. All Chandra observations in this work were reprocessed by the *chandra_repro* script using CALDB (Chandra Calibration Database) version 4.5.9. [64], [65]

3.4.3 Reprojecting and making images

If there are more observations of the same object available, it may be advantageous to merge the event files (lists) from multiple observations into a single one. A merged event file may be then used to search for faint sources or low-surface-brightness extended features. A CIAO tool *reproject_obs* is commonly used to reproject a set of observations to a common tangent point and create a merged event file. This file can be then used to create images that are more suitable for studying faint emission than event files from individual observations. However, care should be taken when using this merged product with other CIAO tools, for instance when extracting spectra, since some information may have been lost (e.g. if observations have different response files in the CALDB). The preference is to use the individual event files to create separate data products and then either analyze them simultaneously or combine them. [66], [67]

Reprocessed or merged event files can be used to make images. I used the CIAO tool *dmcopy* to create image files corresponding to the soft, medium, and hard energy bands. In this work the soft band images were made using events in the energy range from 0.2 to 1.5 keV, the medium band correspond to energies from 1.5 to 2.5 keV and the hard band to energies from 2.5 to 8 keV. These images can be then combined into a single RGB image using CIAO or via ds9.[68]

3.4.4 Count estimates, spectral extraction and interpretation

In the case that the presence of X-ray emission from within the stellar bow shock was not visually apparent, a count estimate from within a defined aperture may prove useful as a possible way to detect any enhanced X-ray emission. The source and background elliptical or bean-shaped apertures (regions) were defined in the produced X-ray images with the help of ds9 software. The source apertures were defined as to encompass the mid-infrared bow shock emission. The count information was then extracted from the hard, medium, soft and broadband (0.2-8.0 keV) images using the CIAO tool *dmextract*. [69], [70]

Using the already defined regions (or by defining the new ones in the identical way), it is possible to extract the spectrum of an object. While this can be done manually, the CIAO tool *specextract* is widely used for this task. Since the expected X-ray emission is very faint and in the case there are more observations of the objects available, it is possible to sum multiple spectra of the same object to achieve a better signal-to-noise ratio. This can be done via the *combine_spectra* script. [71], [72], [73], [74].

The obtained spectra were inspected using the XSPEC program. XSPEC is also capable of spectral fitting using many models for almost all conceivable emission and absorption processes in the X-ray band. [75], [76]

Instrument	Bandpass	PSF
	keV	
ACIS-I	0.3-10	0.5
ACIS-S	0.3-10	0.5

Table 3.2: CXO (Chandra) detector specifications.

Application Name	Description
MOPEX	A package for reducing and analyzing the Spitzer imaging data, as well as Spitzer-MIPS SED data. MOPEX also includes the point source extraction package, APEX.
HIPE	An application that allows users to work with the Herschel data, including finding the data products, interactive analysis, plotting of data, and data manipulation.
ds9	An astronomical imaging and data visualization application
HEAsoft	A large software collection including mission-dependent tools for a number of HEA satellites, as well as a suite of mission-independent programs
CIAO	The standard software package for Chandra, required for the analysis of Chandra data
XSPEC	A command-driven, interactive, X-ray spectral-fitting program

Table 3.3: A short overview of software tools and packages used to reduce, analyze and visualize the data that were used in this work.

Chapter 4

The bow shock catalogue and mid-infrared morphology study

When stellar bow shocks were observed for the first time by the previous-century infrared space missions, they appeared as simple, smooth arcs of extended emission. Early theoretical modelling and observational evidence thus pushed the notion that bow shocks should exhibit simple morphologies and any observed clumpiness or other unusual morphological features were used as an evidence against the bow shock interpretation of the arc in question.

However, with the advent of more advanced infrared missions, such as the Midcourse Space Experiment (MSX), or more notably, Spitzer and WISE, bow shocks began showing a more complex structure, such as clumps, filaments or dents in the arcs. These complex morphologies have been linked to large-scale magnetic fields, gradients in the density of the ISM and instabilities developing within bow shocks. Thus it is vital to obtain the highest quality image data when studying stellar bow shocks. On the other hand, these irregular structures make it challenging to precisely determine the structural parameters of the investigated bow shocks in a quantitative way.

In this chapter, I will use the following parameters to characterize the investigated bow shocks:

- the apparent stand-off radius, R_s – measured from the bow shock-driving star to the intercept between the axis of symmetry of the bow shock and its outer edge.
- the bow shock width, w – measured along the axis of symmetry of the bow shock from its inner edge to its outer edge.
- $\pi/2$ radius, $R(\pi/2)$ – the apparent distance from the star to the outer edge of the bow shock measured along the line perpendicular to the bow shock axis of symmetry.

4.1 The sample

As of writing this thesis, there is no such thing as a catalog of known stellar bow shocks or bow shock candidates. Most of the studies address a singular, or at most, couple bow shocks at once. One example of a rare statistical study on bow shocks was conducted using

E-BOSS bow shocks (Peri et al. 2012 [24]), where the occurence of bow shocks and the driving star spectral type, age and mass are investigated. However, the number of bow shocks or bow shock candidates within E-BOSS is too small for any definite conclusions to be drawn. Because of the lack of bow shock catalogs, other avenues of statistical research that can be done on these objects are yet unexplored.

For the needs of this thesis, I have compiled a list of some of the known bow shocks driven by early-type stars from the literature (Kaper et al. 1997 [10], Gvaramadze et al. 2011 [11], Peri et al. 2012 [24], Kobulnicky et al. 2012 [77], Ngoumou et al. 2013 [78], Gvaramadze & Bomans 2008 [79] and Gvaramadze et al. 2011b [80]) . The list (see Table 4.1 and 4.2) will serve as a basis for most of this work. This list is by no means a complete list of all known stellar bow shocks.

The list of bow shocks also indicates the availability of the data from the most modern mid-infrared and X-ray space missions which I utilize in this thesis (the coverage by the XMM Newton data is included as well, but the data obtained by this mission are not used in this work). The observations from these missions were reduced using methods outlined in the previous chapter and science-grade data were obtained.

Considering that all of the observed bow shocks are easily visible in the MIPS 24 μm channel and WISE 22 μm channel images, and only a limited number of them exhibit emission in shorter wavelengths, I use MIPS 24 μm and WISE 22 μm images as a basis for measuring the structural parameters of the observed bow shocks. Since MIPS 24 μm images are superior to WISE 22 μm ones, they are preferred, if available. The list of all reduced Spitzer observations is cointained in Table 4.3.

4.2 Refined E-BOSS bow shocks

The E-BOSS catalog is currently the only bow shock catalog utilizing uniform search criteria and a systematic search process (Peri et al. 2012 [24]). However, the catalog is built around the early-mission WISE image data and sometimes unreliable kinematic data. It is therefore possible to utilize a higher-quality Spitzer data and more precise kinematical data to reveal a more detailed sructure of some bow shock candidates or to compute an improved ISM density estimate. Some bow shocks were excluded, despite being covered by Spitzer, for the following reasons:

- Bow shocks around systems HIP 25923, 62322 and 97796 are covered by the data taken in MIPS phot mode and do not appear to provide a better spatial resolution than WISE images.

- Bow shocks associated with HIP 26397, 34536, 101186 and BD +43 are not observed by MIPS and have only the post-cryo (PC) IRAC data available. Observations in the post-cryo mode utilize only the first two IRAC channels (3.6 and 4.5 μm) and only a small number of known bow shocks are visible in such short wavelengths. These four bow shocks are not visible in the images made from the IRAC PC data.

- ζ Oph is a well-known and studied bow shock and will not be discussed here.

Object	IRAC	MIPS	PACS	*Chandra*	XMM
Vela X-1	•	•	•	•	•
4U 1907+09	•	•	•		•
4U 1258-61			•		
EXO 1722-363	•	•	•		•
α Cam	•	•	•		
AE Aur	•	•			•
ζ Oph	•	•	•	•	
AX J1226.8-6249	•	•	•	•	•
HIP 2036					
HIP 2599	•	•	•		
HIP 11891	•	•	•	•	•
HIP 16518					
HIP 17358					
HIP 25923		•			•
HIP 26397	•		•		
HIP 28881					
HIP 29276					
HIP 31776					
HIP 32067			•		
HIP 34536	•		•		
HIP 38430	•	•			
HIP 62322		•			
HIP 72510					
HIP 75095	•	•	•		
HIP 77391					
HIP 78401					
HIP 82171					
HIP 88652					
HIP 92865					
HIP 97796		•			
HIP 101186	•				
BD +43 3654	•		•		•
HIP 114990	•	•	•		

Table 4.1: Catalogued and suspected bow shock producing systems and their data coverage by various instruments or surveys (first part).

To facilitate better comparison to Peri et al. (2012 [24]) I keep the same orientation of the images. I also adopt a similar color mapping: blue= 3.6 μm, green = 8.0 μm and red = 24 μm. Using the tabulated values for the proper motions and radial velocities from the paper, I compute the total peculiar velocities (see [38] for the tangential peculiar velocity calculation cookbook and equation (14) from Gies & Bolton 1986 [81] to calculate the radial peculiar velocities). I ignore the solar peculiar motion when computing the radial peculiar velocities, since this will introduce an error at most v = 16 km s^{-1} (normally

much lower than this in the most cases). Since the adopted values from [24] do not have uncertainities associated with them and the typical errors in tangential peculiar velocity determinations are usually much larger than this, the error arising from ignoring the solar peculiar motion can be safely ignored. The parameters of bow shocks determined from the Spitzer images are listed in Table 4.4. I also list the computed peculiar velocities and ambient density of ISM estimates.

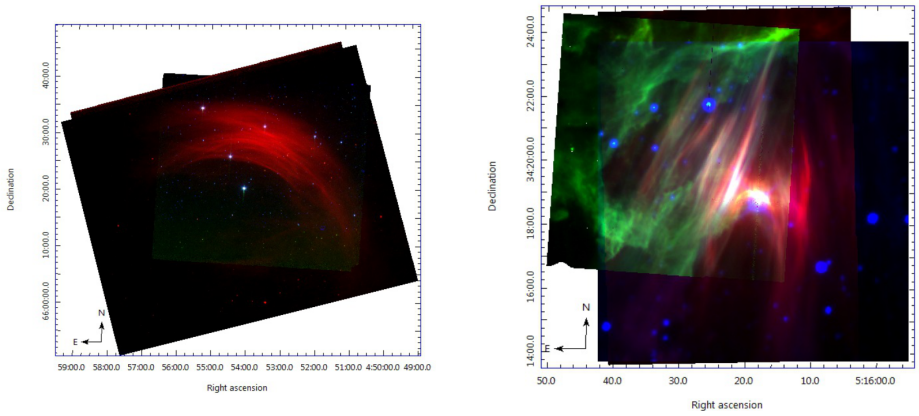

Figure 4.1: Left: bow shock around α Cam, right: bow shock around AE Aur. Since the area was not covered by IRAC 3.6μm data, WISE 3.4μm was used as the blue component for the color composite image of AE Aur.

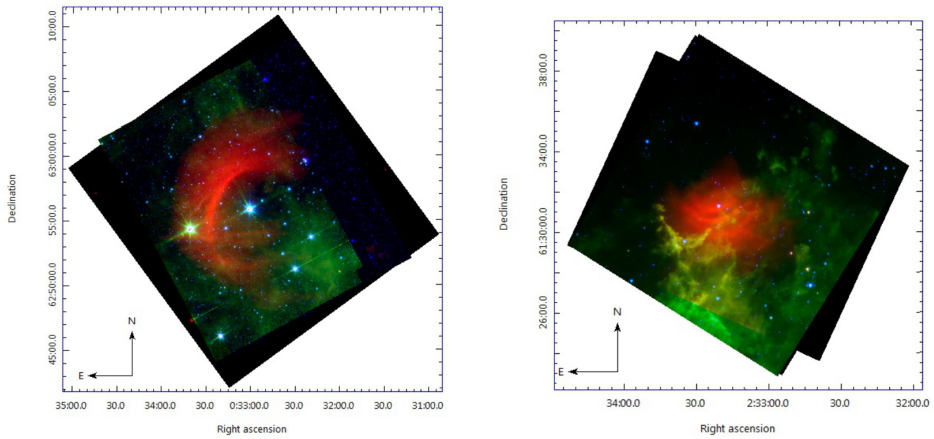

Figure 4.2: Left: bow shock around HIP 2599, right: bow shock around HIP 11891.

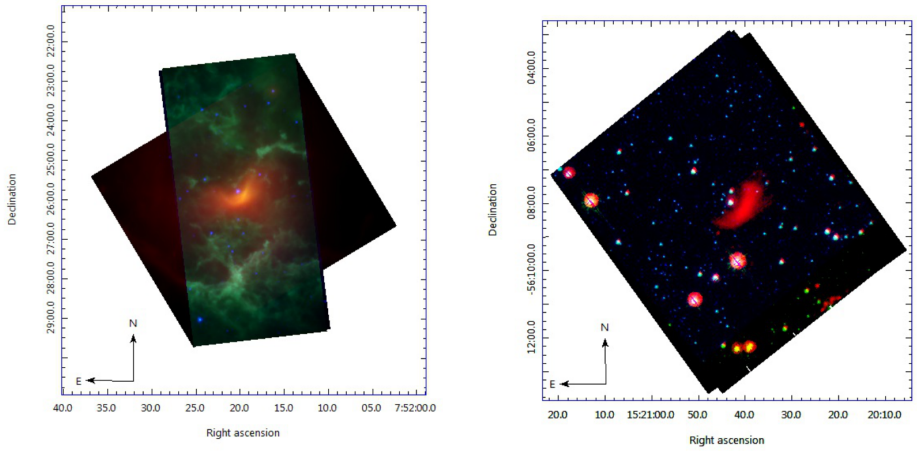

Figure 4.3: Left: bow shock around HIP 38430, right: bow shock around HIP 75095.

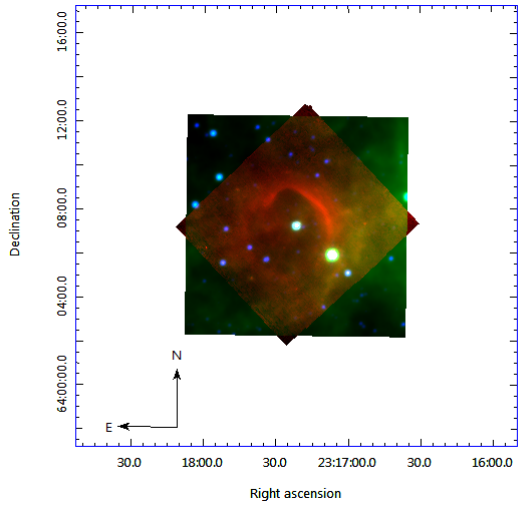

Figure 4.4: Left: bow shock around HIP 114990. Since no IRAC data were available, WISE images were used for the green and blue channels instead.

4.3 Deviations from the prescribed shape

Despite the fact that the agreement with the classical bow shock shape of Wilkin (1996 [34]) has been used to determine the nature of the bow shock candidates (e.g. Kobulnicky et al. 2010 [39]), it became increasingly noticable that many of the most well-known bow shocks do not exhibit the morphology consistent with Wilkin's prescription (e.g Gvaramadze et al. 2011 [11]). To investigate this, I produced synthetic bow shock outlines based on analytical shape parametrization of Wilkin (1996 [34]) and overlaid them on mid-infrared two color images of the seleted bow shocks (see Figure 4.5). Since the morphologies of the bow shocks are quite complex, and moreover, they are embedded within diffuse emission,

it seems impossible to use any quantitative way to fit the analytical shapes. The fits are thus done using visual examination. It is visible that there are indeed obvious disagreements between the analytical shape and observations, especially further from the bow shock axis of symmetry.

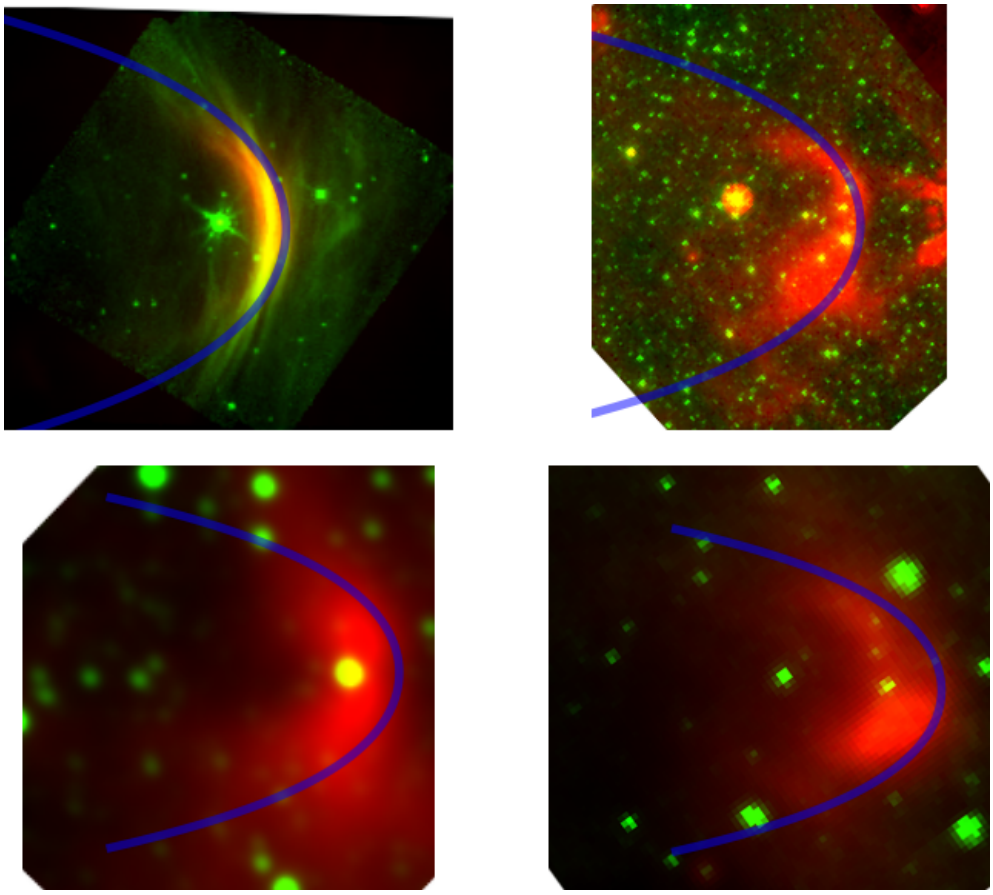

Figure 4.5: Images of the infrared arcs around HMXBs with theoretical bow shocks, based on analytical shape parametrization of Wilkin (1996), plotted in blue. Top left: Image of the arc around Vela X-1 with 24μm light in red and 8μm light in green. Top right: Image of the arc around 4U 1907+09 with 24μm light in red and 8μm light in green. Bottom left: Image of the arc around 4U 1258-61 with 22μm light in red and 3.4μm light in green. Bottom right: Image of the arc around EXO 1722-363 with 24μm light in red and 8μm light in green.

While this has been previously noted, no one has yet investigated this problem on a larger number of bow shocks. It may be interesting to search for possible correlations between the shape deviation (observed - computed, $O-C$) and stellar wind properties, peculiar velocities and visibilities in the various bands. For this task, I selected some suitable bow shocks from my initial sample. Bow shocks covered by the high-resolution data were preferred, since it was necessary to reliably determine R_s and $R(\pi/2)$. This was doable only when $R_s > w$, which was mostly the case for the close bow shock systems or the systems covered by the Spitzer observations. I measured $R(\pi/2)$ for both flanks of the bow shock. Since the density gradients in the ISM and asymetric stellar winds may slightly

displace the star from the axis of symmetry of the bow shock, the average of both values was taken. These values were expressed in the dimensionless units of R_s and are tabulated in Table 4.5. Since the finite width of the bow shock cannot be ignored, I recommend to use the values with caution and adopt a relative error of at least 20%.

From Table 4.5, it is readily apparent that it is not advisable to use the analytical bow shock shapes to distinguish between the stellar bow shocks driven by early-type stars and other arcuate objects visible in the mid-infrared bands. In the most extreme cases, the deviations from the analytical shape at the right angles to the bow shock axis of symmetry are comparable to the apparent stand-off radius, R_S itself. I investigate whether the observed deviations depend on the values of the mass loss $\dot{M}$, terminal stellar wind velocity v_∞, or the product of these two parameters. It would be more interesting to also include the stellar peculiar velocities, but these are determined with a very low significance and thus are not usable in any serious analysis.

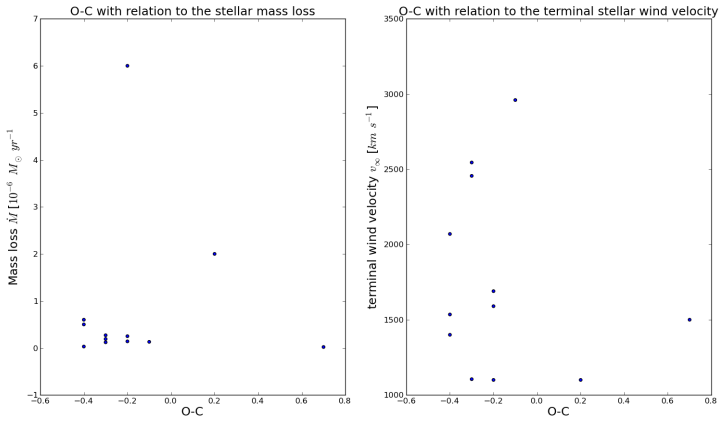

Figure 4.6: The observed deviations $O-C$ (in units of R_s) from the analytical bow shock shape at the right angles to the bow shock axis of symmetry. Left: relation to the stellar mass loss $\dot{M}$, right: relation to the terminal stellar wind velocity v_∞.

Graphs 4.6 and 4.7 visualize the relations between these quatities and the $O-C$ deviations. However, no dependence between these quantities is apparent for both graphs. It is interesting that the bow shocks with high and positive $O-C$, namely those associated with ζ Oph and Vela X-1 are clearly visible in all IRAC channels and the first two short-wavelength WISE channels, while the other objects are not (though bow shocks around HIP 88652 and 2MASS J18152396-1319358 exhibit a faint emission in the WISE 4.6 μm channel).

It may be interesting to investigate whether this visibility and $O-C$ correlation is connected to the nature of the outer layers (i.e. whether they are adiabatic or radiative) of the studied bow shocks. To determine this, we can use the characteristic time-scale for radiative cooling of the gas,

$$t_{cool} \simeq \frac{3kT}{n_{ps}\Lambda(T)}, \tag{4.1}$$

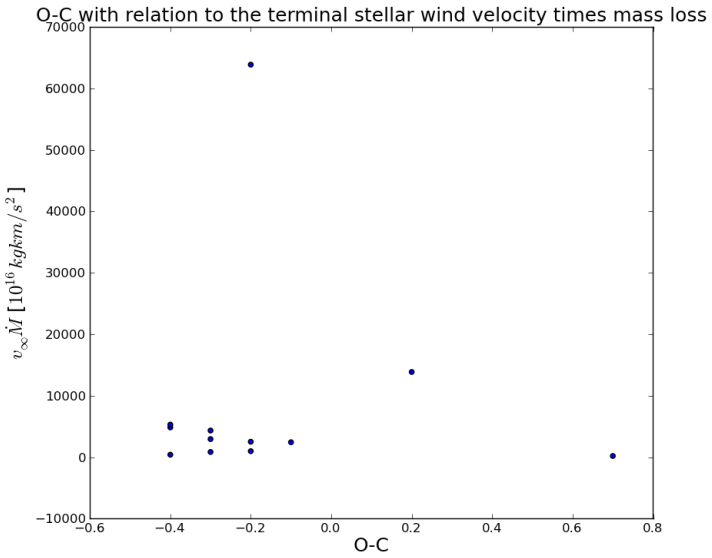

Figure 4.7: The dependence of $v_\infty \times \dot{M}$ on the observed deviations $O-C$ (in units of R_s) from the analytical bow shock shape at the right angles to the bow shock axis of symmetry.

and the characteristic dynamical time-scale of the bow shock,

$$t_{dyn} \sim \frac{R_s}{v_{pec}}, \tag{4.2}$$

where k is the Boltzmann constant, T_{ps} and n_{ps} are the initial post-shock temperature and number density (both can be estimated using the stellar wind and bow shock parameters) and $\Lambda(T)$ is the cooling function. [11]

Gvaramadze et al. (2011 [11]) find, that $t_{cool} \ll t_{dyn}$ for the outer layer of the bow shock around Vela X-1 (having a positive $O-C$) and $t_{cool} \sim t_{dyn}$ for the outer layer of the bow shock around 4U 1907+09 (having a negative $O-C$). Thus the outer layer of the bow shock produced by 4U 1907+09 is adiabatic while that of the bow shock associated with Vela X-1 is radiative. This is consistent with the fact that only the Vela X-1 bow shock manifests itself in Hα, while the one around 4U 1907+09 does not.

This method can be used to determine the time scales for the bow shock associated with ζ Oph (also having a positive $O-C$ and its outer layer may be radiative), however, this star may be affected by the weak-wind problem, so the stellar wind parameters are uncertain. Thus it is not possible to estimate the characteristic time scales. The presence of the Hα bow shock emission also cannot be ascertained, since the system lies within a bright H II region, which dominates the images in the Hα band. The time scales are also hard to determine for the rest of the bow shocks, mainly due to the low significance of the computed stellar peculiar velocities. A dedicated and more precise proper motion measurements of the bow shock-driving stars and a possible future resolution of the weak-wind problem affecting some early-type main sequence stars might enable us to determine these time scales with a sufficient accuracy to reach a conclusion.

4.4 Bow shocks via Herschel

The Herschel Space Observatory has previously been used to study the stellar bow shocks around evolved stars with considerable success (e.g. Ladjal et al. 2010[82], Cox et al. 2012[83]). Despite this, bow shocks associated with early-type stars received little attention. Several of the bow shocks included in the sample are covered by the public Herschel PACS data. In this section, I investigate far infrared counterparts to bow shocks and bow shock candidates driven by high-mass X-ray binaries (HMXBs). The resulting images are presented in Figures 4.8 to 4.11.

The visibility of bow shocks in the far infrared depends on the brightness of the bow shocks and complexity of the background. All bow shocks are visible in the blue 70 μm PACS channel. For instance, the bow shock driven by Vela X-1 is clearly seen in all PACS bands (see Figure 4.8). On the other hand, a fainter bow shock around the system 4U 1258-61 shows a morphology comparable to its mid-infrared counterpart only in the blue PACS channel, the longer-wavelength images reveal some other extended structure in this area, with a morphology that does not correspond to the bow shock as observed in the WISE 22 μm channel. Since this HMXB system lies behind the dark CoalSack nebula, it is possible that the foreground emission from the dark clouds between the observer and the system starts to become more prominent as the wavelength increases, eventually covering up the faint bow shock emission (see Figure 4.10). The visibility of bow shocks around early-type stars in the PACS bands shows considerable promise for the future studies (and possibly even surveys) of these objects.

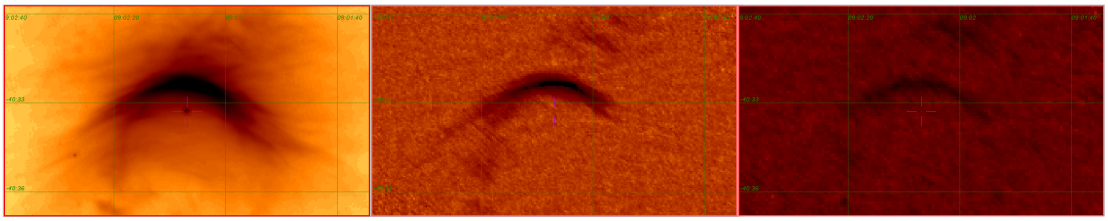

Figure 4.8: From left to right: MIPS 24, PACS 70 and PACS 160 μm images of the field surrounding the HMXB Vela X-1. The position of the system is indicated by a cross. The bow shock morphology is clearly discernable. North is up, east is to the left.

Table 4.6 gives the estimates of the far infrared emission of the bow shocks and bow shock candidates driven by HMXBs. To measure the flux, a bean-shaped or an eliptical aperture encompassing the bow shock emission was constructed and the total flux within the aperture was determined. This is quite straightforward, since the units of PACS maps are Jy/pixel. This ensures that the end product of the photometry will be expressed in (flux/pixel)*pixel = flux units. The same procedure was applied to determine the background level. After the background substraction, the flux was multiplied by $1/EEF$ (Encircled Energy Fraction). The choice of a suitable value of EEF is difficult for the extended source photometry. I calculated the radius of the corresponding circular aperture r_{ap} from the total area of my custom, irregular aperture for each case. Then a tabulated value (given in [84]) of EFF corresponding to the calculated r_{ap} was used. The background in the vicinity of bow shocks was quite complex and its intensity varied wildly. A lot of

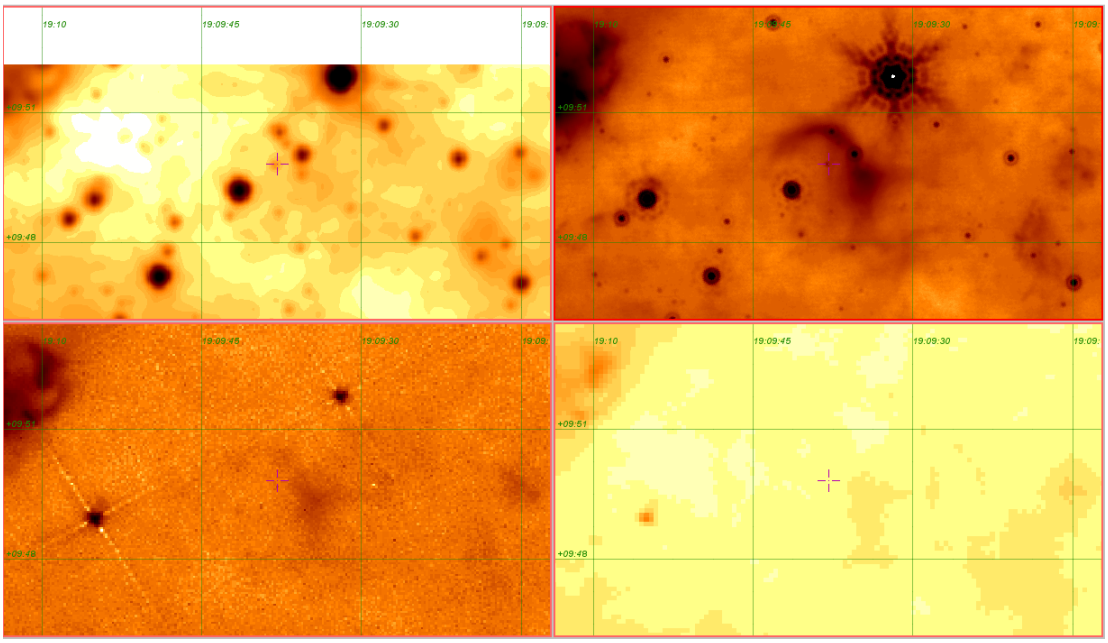

Figure 4.9: From left to right, from top to bottom: WISE 12, MIPS 24, PACS 70 and PACS 160 μm images of the field surrounding the HMXB 4U 1907+09. The position of the system is indicated by a cross. The bow shock morphology is clearly discernable in MIPS 24 and PACS 70 μm. Traces of the bow shock are visible in the WISE 12 and PACS 160 μm images. A bright source 2.5 0.3′ NW is the maser source IRAC19071+0946. North is up, east is to the left.

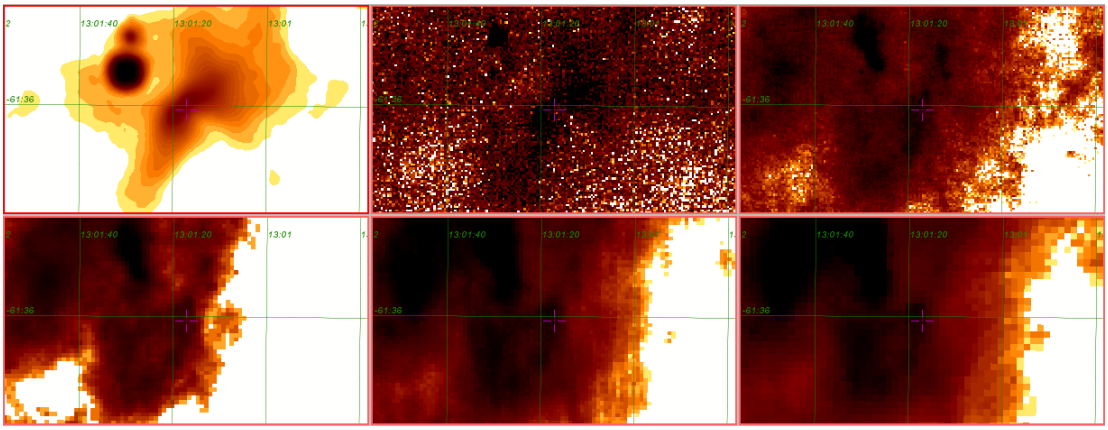

Figure 4.10: From left to right, from top to bottom. WISE 22, PACS 70, PACS 100, PACS 160, SPIRE 250 and SPIRE 350 μm images of the field surrounding the HMXB 4U 1258-61. The position of the system is indicated by a cross. The bow shock morphology is clearly discernable in WISE 22 and PACS 70 μm. A bright source (visible in the WISE 22 μm) to the northeast of the system is the star IRAS 12583-6118. North is up, east is to the left.

bow shocks are located within regions of enhanced emission. Thus, it was very difficult to determine background levels. This severely affects the precision of the photometry, with

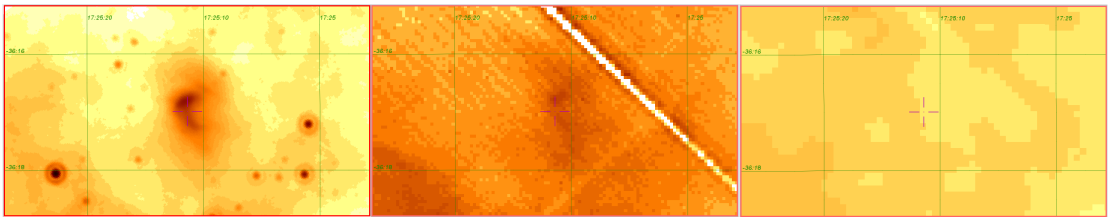

Figure 4.11: From left to right: MIPS 24, PACS 70 and PACS 160 μm images of the field surrounding the HMXB EXO 1722-363. The position of the system is indicated by a cross. The bow shock morphology is clearly discernable in MIPS 24 and PACS 70 μm. The white streak in the PACS 70 μm image is an artifact caused by a bright blob of extended emission 5′ NE of the system. North is up, east is to the left

the background determination being the dominant source of errors. In addition to that, PACS is primarly used for the point-source photometry and there exists no documentation dealing with the analysis of extended sources, further complicating this issue. Thus, the tabulated values should be used with some caution.

The far infrared fluxes can be used to estimate the total dust mass contained in the bow shock (or the total mass of the bow shock, if some dust-to-gas ratio is considered, see Cox et al. 2012[83]). This also requires the distance to the object, dust temperature and dust opacity to be known. Especially the two latter ones are difficult to determine. The dust temperature is not well constrained by the data, since the bow shocks are visible only in a couple of channels and the spectral measurements are almost non-existent. Also the dust opacity is highly dependent on the precise chemical compostion of the dust. The dust temperature can also be estimated using several available dust models, however, these models also heavily rely on the knowledge of the dust chemical composition and dust grain radii. The situation is even more complicated, because unlike many stellar bow shocks around evolved stars, the bow shocks around early-type stars are not visible in the SPIRE bands, which makes it difficult to reliably determine these parameters. Cox et al. 2012[83] adopt an approximate dust temperature $T_{dust} = 35$ K to make their estimates, however, the dust in the bow shocks around HMXBs probably has significantly different temperatures, so I avoid making any estimates.

Object	IRAC	MIPS	PACS	*Chandra*	XMM
IRAS 03063+5735	•		•		
2MASS J10440508-5933412	•	•	•	•	•
BD -14 5040	•		•	•	•
2MASS J18152396-1319358					
2MASS J17271123-3414349	•	•	•		
2MASS J17220342-3414241			•		
HD 319881	•	•	•		
2MASS J17181540-3400061					
N78 34	•	•	•		
2MASS J17225002-3403223			•	•	
2MASS J17271253-3330399	•	•	•		

Table 4.2: Catalogued and suspected bow shock producing systems and their data coverage by various instruments or surveys (second part)

System	AOR	Mode
Vela X-1	17772032	MIPS Scan
	17858560	MIPS Phot
	17858304	IRAC Map
4U 1907+09	15600384	MIPS Scan
	11973376	IRAC Map
EXO 1722-363	20484608	MIPS Scan
	14321152	IRAC Map
α Cam	17771264	MIPS Scan
	17774592	IRAC Map
AE Aur	16032768	MIPS Scan
	16033280	IRAC Map
ζ Oph	17771520	MIPS Scan
	17774848	IRAC Map
AX J1226.8-6249	15659776	MIPS Scan
	15647744	MIPS Scan
	11766528	IRAC Map
HIP 2599	17772288	MIPS Scan
	17775104	IRAC Map
HIP 11891	10498048	MIPS Scan
	13846016	IRAC Map
HIP 25923	14227456	MIPS Phot
HIP 26397	32855552	IRAC Pc
HIP 34536	39073024	IRAC Pc
HIP 38430	15054592	MIPS Phot
	15054336	IRAC Map
HIP 62322	22785792	MIPS Phot
HIP 75095	15588864	MIPS Scan
	9335552	IRAC Map
HIP 97796	19948032	MIPS Phot
HIP 101186	39312640	IRAC Pc
BD +43 3654	39490048	IRAC Pc
HIP 114990	25312256	MIPS Phot
	25311488	IRAC Map
IRAS 03063+5735	32851456	IRAC Pc
2MASS J10440508-5933412	23788288	MIPS Scan
	23695360	IRAC Map
BD -14 5040	12108288	IRAC Map
2MASS J17271123-3414349	20484864	MIPS Scan
	14292736	IRAC Map
HD 319881	20485376	MIPS Scan
	14322432	IRAC Map
N78 34	20483328	MIPS Scan
	14321408	IRAC Map
2MASS J17271253-3330399	20484864	MIPS Scan
	14293248	IRAC Map

Table 4.3: Reduced Spitzer datasets.

System	l [arcmin]	w [arcmin]	R_S [arcmin]	v_{pec} [km s^{-1}]	n [cm^{-3}]
α Cam	44	10	15	60	0.06
AE Aur	1.3	0.4	0.4	140	4
HIP 2599	9.0	0.6	3.3	-	-
HIP 11891	1.8	0.2	0.2	-	-
HIP 38430	0.9	0.3	0.4	-	-
HIP 75095	2.0	0.4	0.7	27	20
HIP 114990	4.0	0.4	1.5	114	0.4

Table 4.4: As in Table 4. of Peri et al. (2012 [24]).l ($= 2 \times R(\pi/2)$) stands for the length of the bow shock structure, w is the width, v_{pec} is the peculiar velocity of the star and n is the ambient density of ISM.

System	$R(\pi/2)$ [R$_S$]	O-C [R$_S$]	$\dot{M}$ [10^{-6} M$_\odot$ yr^{-1}]	v_∞ [km s^{-1}]
Vela X-1	1.9	0.2	2	1100
4U 1907+09	1.5	-0.2	6	1690
α Cam	1.5	-0.2	0.25	1590
ζ Oph	2.4	0.7	0.02	1500
HIP 2599	1.4	-0.3	0.12	1105
HIP 28881	1.3	-0.4	0.03	2070
HIP 32067	1.6	-0.1	0.13	2960
HIP 34536	1.4	-0.3	0.19	2456
HIP 72510	1.4	-0.3	0.27	2545
HIP 78401	1.5	-0.2	0.14	1100
HIP 88652	1.3	-0.4	0.5	1535
HIP 114990	1.3	-0.4	0.6	1400
BD -14 5040	1.3	-0.4	-	-
2M J18152396-1319358	1.5	-0.2	-	-
2M J17271123-3414349	1.3	-0.4	-	-

Table 4.5: Measured deviations and parameters of selected bow shock-producing systems. Mass-loss and stellar wind velocities are taken from [24] and [11]. The abbreviation '2M' stands for 2MASS objects.

	Vela X-1	4U 1907+09	4U 1258-61	EXO 1722-363
Obs Id	1342244881	1342207052	1342189081	1342214575
	1342244882	1342207053	1342189082	1342214576
PACS 70 [Jy]	27.5	6.8	4.1	11.5
PACS 70 S/B	3.1	2.3	~ 1	3.8
PACS 160 [Jy]	7.1	-	-	-
PACS 160 S/B	11.2	-	-	-

Table 4.6: Observed fluxes of the extended bow shock emission around HMXBs. PACS 70 and PACS 160 stands for the net measured fluxes in PACS 70 μm band and 160 μm. The S/B ratio stands for source-to-background, i.e. the ratio of the flux in the source aperture and in the background aperture, determined for each band.

Chapter 5

A candidate bow shock near 2MASS J17222408-3708484

When I was examining the quality of my reduced data of the HMXB system EXO 1722-363 and comparing them to image products obtained from MIPSGAL survey, I noticed an arcuate structure of extended emission with a point source on its axis of symmetry just one degree of arc from the HMXB in one of the MIPSGAL products.

I queried the Spitzer Heritage Archive, WISE Image Service and Herschel Science Archive for all available infrared data for this object. There are IRAC, MIPS and WISE observations covering this object. Unfortunately, no Herschel data is available. The observational data was then processed using the methods discussed in the previous sections.

I also obtained the relevant information about the star driving the tentative bow shock. The star is not yet included in Simbad Astronomical Database despite being visible in the optical band, however, there are several catalogues found via VizieR Service that cover this object. I will use a designation 2MASS J17222408-3708484 for this source, as given by 2MASS All-Sky Catalog of Point Sources (Cutri et al. 2003 [85]). Anderson at al. (2014)[86] also report a candidate H II region (G350.455-00.385) with radius 270 arsec centered just 50 arcsec from 2MASS J17222408-3708484.

5.1 Infrared arc

The infrared arc appears only in the MIPS 24.0 μm images. While there is also a significant emission present in the WISE W4 (22 μm), the lower resolution of WISE does not allow the fine arcuate shape of the bow shock to be resolved. Instead, it only appears as a blob of extended emission and the inspection of the WISE data exclusively would not have yielded a bow shock detection. The candidate bow shock does not have a shorter-wavelength counterpart in any of the Spitzer or WISE bands. The arc exhibits a smooth structure, with the axis of symmetry suggesting that the star driving the bow shock is moving almost parallel to the Galactic equator. The rest of the properties of the bow shock are summarized in Table 5.4.

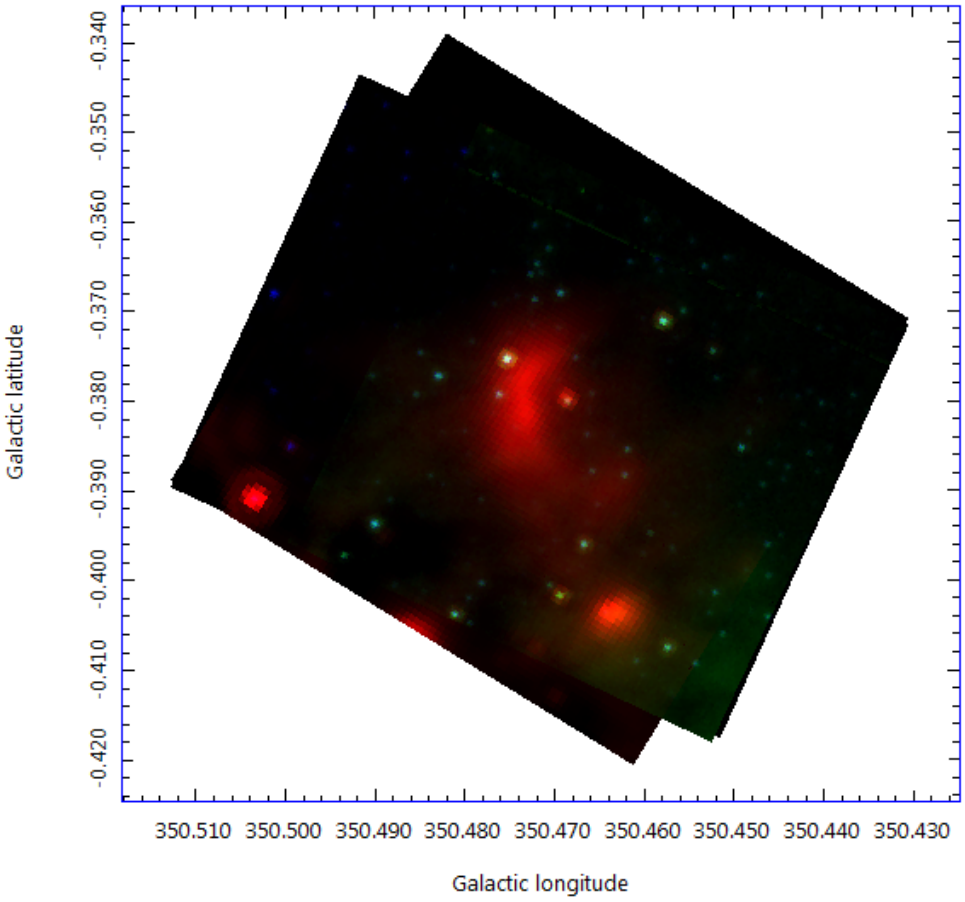

Figure 5.1: Composite 3-color image of the bow shock candidate around 2MASS J17222408-3708484 ((blue = 4.5 μm, green = 8.0 μm, red = 24.0 μm).

band	flux [mJy]
2MASS J	39.8
2MASS H	77.5
2MASS Ks	87.4
IRAC 3.6 μm	56.1
IRAC 4.5 μm	35.9
IRAC 5.8 μm	28.8
IRAC 8.0 μm	25.9

Table 5.1: 2MASS J17222408-3708484 infrared fluxes. (GLIMPSE Source Catalog (I + II + 3D), IPAC 2008)[87]

5.2 Proper motion and peculiar velocity

The axis of symmetry of the bow shock around 2MASS J17222408-3708484 suggests that the system is moving along the Galactic plane. To confirm that the origin of the bow shock is due to a high space velocity of the system, I searched for the proper motion measurements

for this star using Vizier catalogue access tool.

There are several proper motion catalogs listing the proper motion of the star. However, all of them give wildly different values which cannot be easily reconciled. All of them give proper motions that differ significantly from one another and some of them have the measurement uncertainities exceeding or comparable to the measurements themselves. Those are UCAC4 (Zacharias 2012)[88] and SPM 4.0 (Girard 2011)[89] and are not used in the subsequent analysis. Thus, I only use the values given by PPMXL (Roser 2010)[90] and NOMAD (Zacharias 2005)[91]. Using the Galactic constants $R_0 = 8.0$ kpc and $\Theta_0 = 240\,\mathrm{km\,s^{-1}}$ (Reid et al. [92], Gvaramadze et al. [11]) and the solar peculiar motion $(U_\odot, V_\odot, W_\odot) = (10.0, 11.0, 7.2)\mathrm{km\,s^{-1}}$ (McMillan & Binney [93]), I compute the peculiar velocity of the system using the workflow described in Mdzinarishvili & Chargeishvili ([94]). Since the distance to 2MASS J17222408-3708484 is not known, I list the peculiar velocities for a set of possible distances. The errors in the peculiar velocity are computed from the errors of proper motion measurements so they should be considered as low-limit approximations.

μ_α [mas/yr]	μ_δ [mas/yr]	catalogue
-2.4 ± 10.0	1.2 ± 10.3	UCAC4 (Zacharias 2012)[88]
0.19 ± 9.02	-20.20 ± 9.49	SPM 4.0 (Girard 2011)[89]
20.4 ± 18.5	46.5 ± 18.5	PPMXL (Roser 2010)[90]
47.4 ± 9.0	-44.9 ± 9.0	NOMAD (Zacharias 2005)[91]

Table 5.2: Proper motions of 2MASS J17222408-3708484

	distance [kpc]	PPMXL	NOMAD
$(v_{lt})_{\mathrm{pec}}$ [$\mathrm{km\,s^{-1}}$]	0.5	131 ± 44	-11 ± 21
$(v_{bt})_{\mathrm{pec}}$ [$\mathrm{km\,s^{-1}}$]	0.5	30 ± 44	-145 ± 21
$(v_t)_{\mathrm{pec}}$ [$\mathrm{km\,s^{-1}}$]	0.5	135 ± 62	146 ± 30
$(v_{lt})_{\mathrm{pec}}$ [$\mathrm{km\,s^{-1}}$]	1.0	250 ± 88	-34 ± 43
$(v_{bt})_{\mathrm{pec}}$ [$\mathrm{km\,s^{-1}}$]	1.0	53 ± 88	-299 ± 43
$(v_t)_{\mathrm{pec}}$ [$\mathrm{km\,s^{-1}}$]	1.0	255 ± 124	300 ± 60
$(v_{lt})_{\mathrm{pec}}$ [$\mathrm{km\,s^{-1}}$]	1.5	369 ± 132	-58 ± 64
$(v_{bt})_{\mathrm{pec}}$ [$\mathrm{km\,s^{-1}}$]	1.5	75 ± 131	-451 ± 64
$(v_t)_{\mathrm{pec}}$ [$\mathrm{km\,s^{-1}}$]	1.5	376 ± 186	455 ± 91

Table 5.3: Computed peculiar tangential velocities for distances up to 1.5 kpc based on PPMXL and NOMAD catalogs $(v_{lt})_{pec}$ stands for peculiar tangential velocity in the direction of Galactic longitude, $(v_{bt})_{pec}$ for peculiar tangential velocity in the direction of Galactic latitude and $(v_t)_{pec}$ is the total peculiar tangential velocity)

While the kinematic data for this system is very conflicting and unreliable, it can be noted that the direction of motion of the star derived from the PPMXL data corresponds well to the direction of motion inferred from the axis of symmetry of the arc, while the direction of motion derived from the NOMAD kinematic data is almost at the right angle to the axis of symmetry of the arc.

Under the assumption that either PPMXL or NOMAD give physically sensible data, it is possible to constrain the distance to the star. Regardless of whether the arc around 2MASS J17222408-3708484 is actually a stellar bow shock or a dust wave, both of these objects form almost exclusively around O and early B type stars. Therefore, 2MASS J17222408-3708484 is likely an early type star. Tauris (2014 [95]) showed that in the case of binary supernova ejection scenario and even under the most favorable conditions, a runaway early B star should not exceed the peculiar velocity $(v)_{pec} = 320\mathrm{km\,s^{-1}}$. Thus, according to PPMXL, 2MASS J17222408-3708484 should be no further than approximately 1.5 kpc. NOMAD suggests even lower distance limit of about 1 kpc. In greater distances the computed peculiar velocities become unphysical. However, it should be noted that the other catalogs report much smaller peculiar motion, so these limits must be treated with caution and the actual distance to the star may be much greater. A more precise, dedicated astrometrical study of this star is very much needed.

5.3 Interpretation of the arc

The point source associated with the arc does not exhibit rising flux levels towards longer infrared wavelengths which are typical for young stellar objects. Thus I can rule out the possibility that the arc is a remnant of a dusty gas column which was previously a site of a stellar formation. Infrared arcs with a star on or near their axis of symmetry are traditionally interpreted as stellar bow shocks, but Simpson et al. (2014 [96]) report a presence of a candidate interstellar bubble centered near 2MASS J17222408-3708484 (catalog identification 1G350467-003797). This bubble was identified with the help of volunteers under the 'The Milky Way Project'. However, the bubble was identified only by a small fraction of them (hit rate of 18 %). The investigation of 8.0 μm IRAC data that is frequently used to trace such bubbles reveals two rims of emission that could be remnants of an interstellar bubble. Since the bubble is so evolved, any ionized gas flows associated with the pierced bubbles must have long dissipated, but the more prominent of the rims may still fuel the dust wave. The orientation of the arc is consistent with this possibility. This means that the arc may be a dust or a bow wave. Possible future spectroscopic studies of the driving star or the infrared arc may give more insight into this problem.

$R_{S,a}$ [arcsec]	40
d [arcsec]	90
t [arcsec]	20

Table 5.4: Characteristics of the arc around 2MASS J17222408-3708484. $R_{S,a}$ stands for apparent stand off radius of the BS, d is the angular size of the BS and t is thickness of the BS measured at its apex..

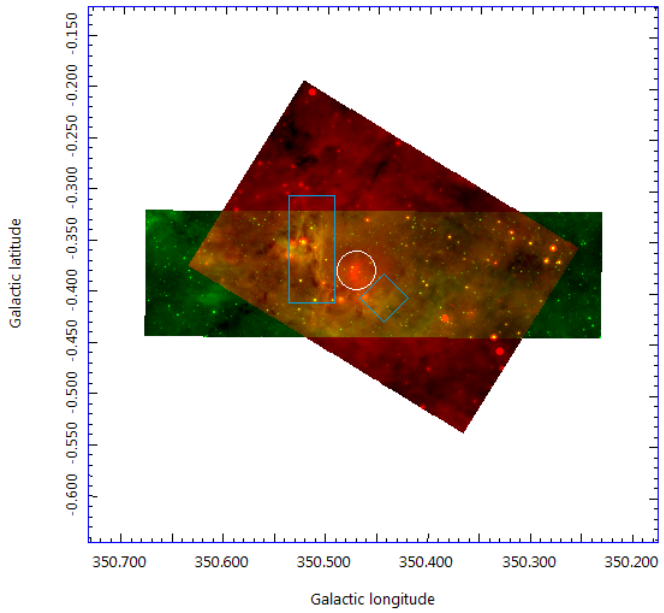

Figure 5.2: Composite 2-color image of wider environs of 2MASS J17222408-3708484 made from the Spitzer data (green = 12 μm and red = 24 μm). The star driving the bow shock is marked by the white circle and the possible bubble remnants are highlighted by blue rectangles.

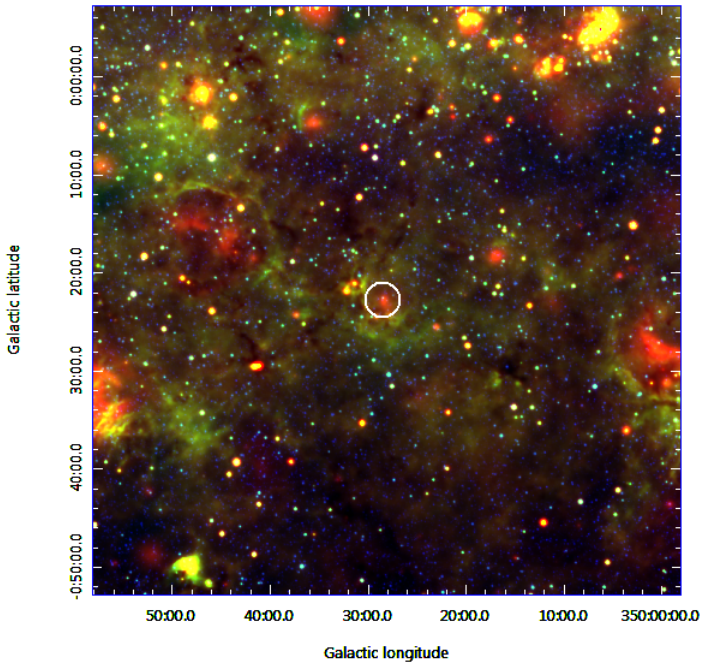

Figure 5.3: Composite 3-color image of wider environs of 2MASS J17222408-3708484 made from WISE data ((blue = 3.4 μm, green = 12 μm, red = 22 μm). The star driving the bow shock is marked by the white circle.

Chapter 6

Bow shocks in high energies

Stellar bow shocks are not among the objects that are of high interest to high-energy astronomers. Thus, X-ray observations of stellar bow shocks are very rare. Most of the observations that I was able to retrieve from the archive were serendipitious, as our objects of interest were only by chance in the field of view of observations done to study a nearby high-energy source, for example a pulsar or a supernova remnant.

Since (as of writing this thesis) the X-ray emission from a stellar bow shock has only been detected once, it is hard to tell how exactly will a bow shock manifest in X-rays. In the case of AE Aur, the X-ray bow shock emission lies embedded inside the mid-infrared emission, but quite far off from the bow shock axis of symmetry. It also can be noted that the X-ray source is much smaller in size than the mid-infrared bow shock. This might mean that only certain parts of a bow shock produce high-energy emission.

Considering the inherent ambiguity resulting from having only one X-ray detection, I consider several scenarios when searching for X-ray emission from bow shocks:

- The presence of an X-ray counterpart to a stellar bow shock may reveal itself in the Chandra broadband images, especially when combined with the mid-infrared data.

- Even if no X-ray emission from the bow shock can be visually detected in the Chandra broadband image, we can use the fact that the bow shock emission probably has different hardness compared to the diffuse X-ray background. Constructing colored images with different colors corresponding to different energies may reveal the presence of X-ray emission of different hardness even if the number of counts is not that higher to the background. This is only sensible to do when the images are not too grainy, meaning the exposure is sufficiently long.

- Using the same principle, we can extract the spectra from a suitably defined aperture and compare it to the background.

- For very distant bow shocks, or for the ones that are very small in size, we can expect a possible X-ray emission to be very close to the emission from the star powering the bow shock and difficult to disentangle. In that case, the spectral analysis of the star may reveal surplus emission at the certain energies that may be caused by the presence of a bow shock.

In this section, I make use of data from the Chandra X-ray observatory, having an unprecedented spatial resolution, shadowing the past or current X-ray observatories. The obtained and reduced list of archive data is contained in Table 6.1.

Target	Obs ID	Obs. date	Exp. time [ks]	Instrument
Vela X-1	102	2000-04-13	28.0	ACIS-S (HETG)
	1928	2001-02-05	29.6	ACIS-S (HETG)
	1927	2001-02-07	29.4	ACIS-S (HETG)
	1926	2001-02-11	83.1	ACIS-S (HETG)
ζ Oph	2571	2002-09-04	35.4	ACIS-S (HETG)
	4367	2002-09-05	48.3	ACIS-S (HETG)
	14540	2013-07-03	72.1	ACIS-I (NONE)
AX J1226.8-6249	103	2000-06-19	39.5	ACIS-S (HETG)
	2733	2002-01-13	39.2	ACIS-S (HETG)
	2734	2001-12-13	59.0	ACIS-S (HETG)
	3433	2002-02-03	59.0	ACIS-S (HETG)
	3811	2003-10-04	3.0	ACIS-S (NONE)
HIP 11891	7033	2006-11-25	80.0	ACIS-I (NONE)
2MASS J10440508-5933412	4495	2004-09-21	57.3	ACIS-I (NONE)
BD -14 5040	4600	2004-07-09	11.0	ACIS-I (NONE)
	5341	2004-07-11	18.0	ACIS-I (NONE)
2MASS J17225002-3403223	13623	2013-02-01	39.5	ACIS-I (NONE)

Table 6.1: Reduced Chandra datasets

6.1 Vela X-1

Vela X-1 is a well-known bow shock-producing supergiant HMXB. Since it is a prominent object of the X-ray sky, it has been of interest to numerous X-ray mission and it has even been used as an X-ray calibration source. There are several Chandra observations of Vela X-1, however, they all utilize gratings. While it is possible to detect background sources in the zero-order images of the grating observations, it is unknown whether the source statistics and/or spectra can be reliably extracted for the background sources in this case. The author is unaware of the Chandra documentation or paper adressing this.

Nevertheless, it is still possible to visually search of any possible X-ray emission. Figure 6.1 shows the broadband Chandra image of Vela X-1 overlaid onto the mid-infrared image and a composite color X-ray image of the same field. I verified that the region used for extraction of the grating spectra (spectral information is contained in the two 'whisker ' almost parallel to the right ascension in Figure 6.1) is well within the bow shock. Thus, the previous investigators studying spectra of Vela X-1 could not have seen any contribution from the bow shock (provided that there is any). I do not detect any notable X-ray emission from within the bow shock in either image of Figure 6.1).

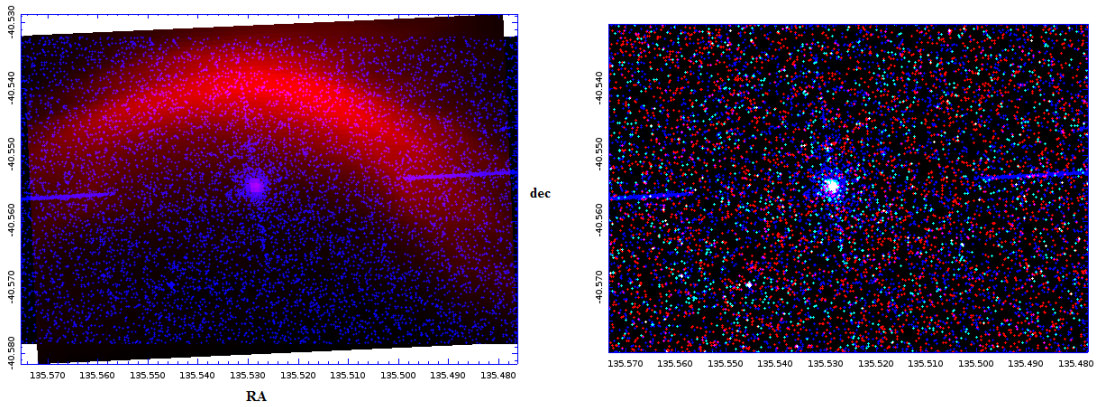

Figure 6.1: Left: A broadband Chandra 0.2-8 keV image of Vela X-1 (in blue) overlaid on Spitzer MIPS 24 μm image (in red). Right: Composite 3-color image of the same field. Red corresponds to energies 0.2-1.5 keV, green to 1.5-2.5 keV and blue to 2.5-8 keV.

6.2 ζ Oph

The early-type star ζ Oph produces perhaps the most well-known stellar bow shock. Since the star is quite bright in X-ray energies, it has been a subject of a couple of grating observations. Oskinova also proposed a 75 ks exposure investigating any possible X-ray emission resulting from non-thermal processes that may indicate effficient acceleration of particles within the shock. This observation is stored in the archive under the Obs ID 14540. According to ADS search querries, no research paper adressing the presence (or lack of thereof) of bow shock X-ray emission associated with ζ Oph was ever published.

The broadband X-ray image of the sky around the apex of the bow shock combined with the MIPS mid-infrared image is shown in Figure 6.2. Despite the long exposure, no obvious point or extended source are visible from within the bow shock.

The count statistics of the sky within the bow shock revealed no excess in broadband or in any other energies. In fact, taken at face values, the count rates of the bow shock are even slightly lower than those of the background (see Table 6.2. Thus I conclude that there is no X-ray emission detectable that is associated with the bow shock around ζ Oph.

band	count rate $[10^{-3}\mathrm{s}^{-1}]$	S/B
broad	-0.51 ± 0.72	< 1
soft	-0.13 ± 0.37	< 1
med	0.10 ± 0.27	1.0
hard	-0.47 ± 0.55	< 1

Table 6.2: Count estimates (with 1-σ error) for the X-ray emission within the arcuate infrared nebula in the position of ζ Oph. S/B stands for approximate ratio between the source and background count rates, .

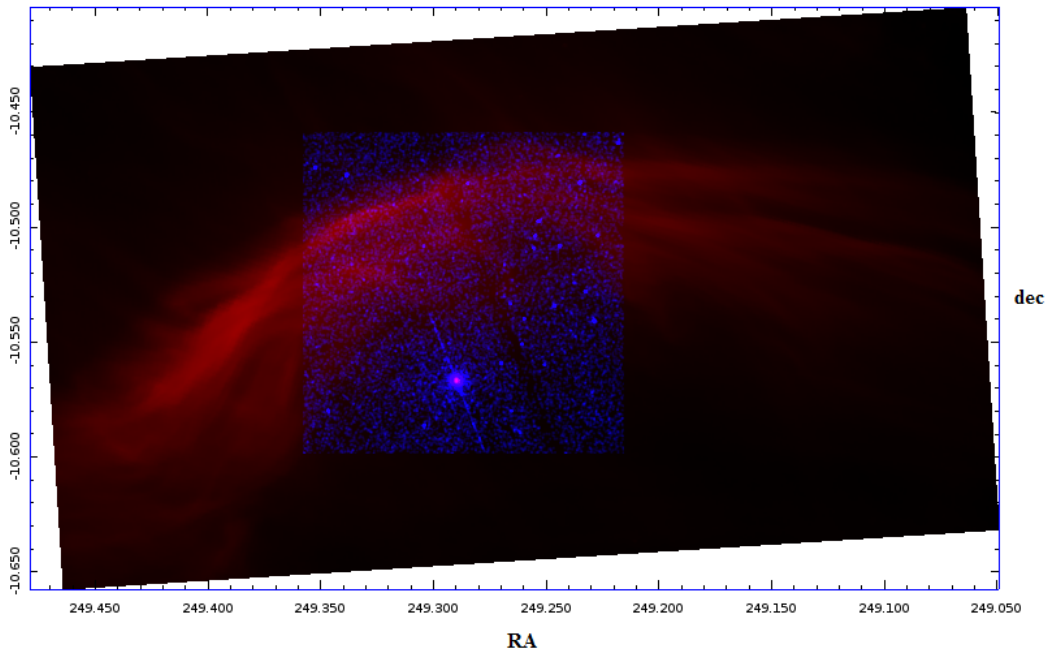

Figure 6.2: A broadband Chandra 0.2-8 keV image of the area around ζ Oph (in blue) overlaid on Spitzer MIPS 24 μm image (in red).

6.3 AX J1226.8-6249

AX J1226.8-6249 is an X-ray source of unknown nature lying in the proximity (approximately 200 arcsec) of a well-known high-mass X-ray binary GX 301-2. The object is mentioned in some papers studying GX 301-2, especially as a possible source of contamination that may affect the analysis of GX 301-2, since the extreme brightness of this HMXB and limited capabilities of earlier X-ray missions meant that the image of GX 301-2 spilled over into adjacent pixels, affecting the area of several arcminutes around it. Pravdo et al. (1995 [97]) disentangled the emission of AX J1226.8-6249 from GX 301-2 and note that the intensity of AX J1226.8-6249 is only at approximately 4% the GX 301-2. Subsequent studies of GX 301-2 also notice the presence of AX J1226.8-6249. Endo et al. (2002 [98]) note that the X-ray spectrum of AX J1226.8-6249 is much softer than that of GX 301-2. The also report a huge difference in brightness of the two sources (the intensity of AX J1226.8-6249 in only 6% of GX 301-2 in the band 2.0-3.0 keV). To the best of author's knowledge, no dedicated studies of AX J1226.8-6249 have not been conducted so far and its precise position, brightness, nature and spectral characteristics are unknown.

In 2002, Eikenberry proposed a 3-kilosecond ACIS-S observation toward the unidentified X-ray source AX J1226.8-6249. Being close to a mid-infrared bow shock nebula, the proposer consider a possibility that AX J1226.8-6249 is in fact a Be/X-ray runaway binary, producing a bow shock via its supersonic motion [99]. However, my search among the peer-reviewed literature for a paper on this topic written by the proposer (or by anyone else) produced no results. This observation is available in the Chandra archive under the Obs ID 3811. The inspection of the images made from this observation are very grainy

and at the first glance, only GX 301-2 (upper right corner of Image 6.3) is readily apparent. However, smoothing the obtained images reveals a compact extended emission in the previously reported approximate position of AX J1226.8-6249. One part of the extended emission is a bit brighter. Combining these images with the images obtained from IRAC and MIPS data reveal that this X-ray emission seems to be immersed within 24μm arcuate nebula. Using IRAC 3.6μm images I attempted to determine possible stellar counterparts. However, the vicinity of AX J1226.8-6249 is so crowded with infrared point sources that this was deemed impossible. Simbad reports only one star in the vicinity (15.2 arcsec) of AX J1226.8-6249. The star (2MASS J12265165-6249199) might be an OB star (Reed 2005 [100]) but the precise spectral classification is unknown. The position of the star corresponds well to the brighter blob of the extended X-ray emission. However, the star apparently lies within the nebula and significantly off its axis of symmetry. Count extimates for the extended source can be found in Table 6.3. The spectrum of the emission was also extracted, but since the brightness of the source is too low and the exposure is too short, no detailed information could be extracted. However, it is apparent that the emission is very soft.

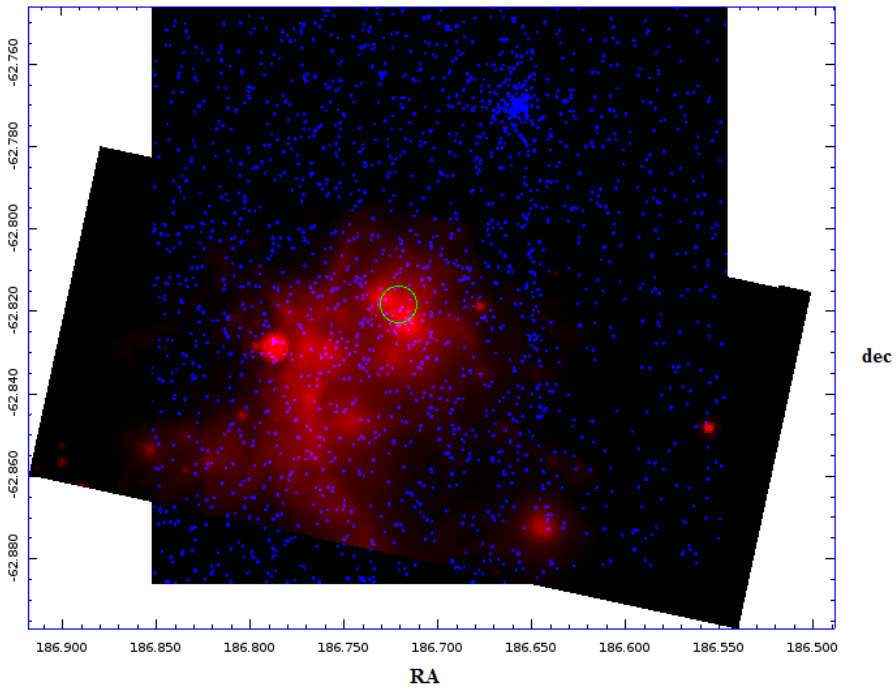

Figure 6.3: A broadband Chandra 0.2-8 keV image of the area around AX J1226.8-6249 (in blue) overlaid on Spitzer MIPS 24 μm image (in red). The Chandra image is derived from observation with the Obs ID 3811. The position of AX J1226.8-6249 is marked by a green circle.

A longer-exposure grating observation with ID 2734 may be used to get a closer look at AX J1226.8-6249, despite its limitations. Figure 6.4 reveals two point X-ray sources, possibly early-type stars, in the approximate position of AX J1226.8-6249. Overlaid onto the mid-infrared emission, it appears that none of them is an X-ray counterpart of the star

band	count rate [10^{-3}s^{-1}]	S/B
broad	8.02 ± 2.06	4.4
soft	4.01 ± 1.49	4.0
med	3.01 ± 1.11	10
hard	1.00 ± 0.88	2.5

Table 6.3: Count estimates for the X-ray emission within the arcuate infrared nebula in the position of AX J1226.8-6249.

driving the bow shock. It is also unlikely that either of them is associated with the bow shock, but this cannot be entirely discounted. They are probably background sources.

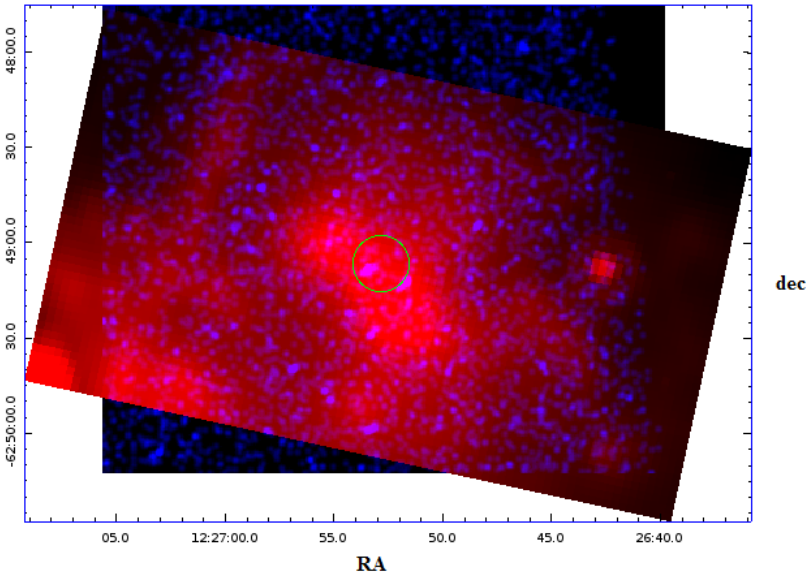

Figure 6.4: Same as in the previous figure but now the Chandra image is made from observation with the Obs ID 2734 which has a significantly higher exposure time. The position of AX J1226.8-6249 is marked by a green circle.

6.4 HIP 11891

The sky around the peculiar bow shock-producing star HIP 11891 is covered by observations of the Heart nebula (IC 1805). Overlaying the X-ray emission onto the mid-infrared image, it is apparent that the X-ray data cover only the parts of the two outer mid-infrared arc around HIP 11891 (see Figure 6.5). Since it is not clear whether these two arcs are actually active bow shocks and only their partial area, far from their apex, is covered, I do not perform any analysis on this object.

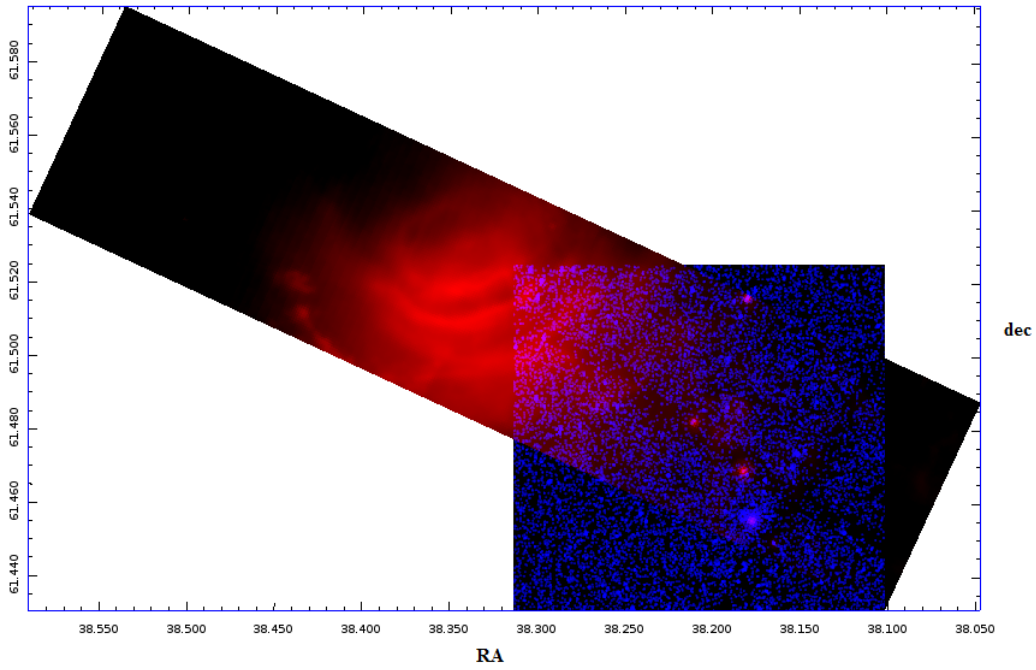

Figure 6.5: A broadband Chandra 0.2-8 keV image of the area around HIP 11891 (in blue) overlaid on Spitzer MIPS 24 μm image (in red). The Chandra image covers only a part of the bow shock.

6.5 2MASS J10440508-5933412

Ngoumou et al. (2013, [78]) detect an X-ray source associated with the bow shock-driving star 2MASS J10440508-5933412. Using 60 ks Chandra observation mapping the Carina nebula, they attribute this emission to the driving star itself. They report an excellent agreements among the mid-infrared stellar couterpart and the X-ray emission and derive an approximate plasma temperature of $kT \approx 2.5$ keV and median photon energy of the source of 1.48 keV. Since the source has already been investigated, I give it no further attention.

6.6 BD -14 5040

BD -14 5040 is an O8V main sequence bow-shock driving star, thought to be expelled from the open cluster NGC 6611 (Gvaramadze & Bomans). This object happens to be in the field of view of two observations studying a nearby supernova remnant. By combining the X-ray broadband image of the sky around BD -14 504 with the mid-infrared data, I identified a point or compact extended blob of X-ray emission on the axis of symmetry of the infrared arc (see Figure 6.6).

I extracted the spectrum of the source using a small elliptical aperture. Since the region is practically devoid of any other notable X-ray sources, I extracted the background spectrum from a circular region placed near the source of interest. It can be seen from the spectra that the source does not radiate outside of the range of 0.5-2.5 keV (see Figure 6.7).

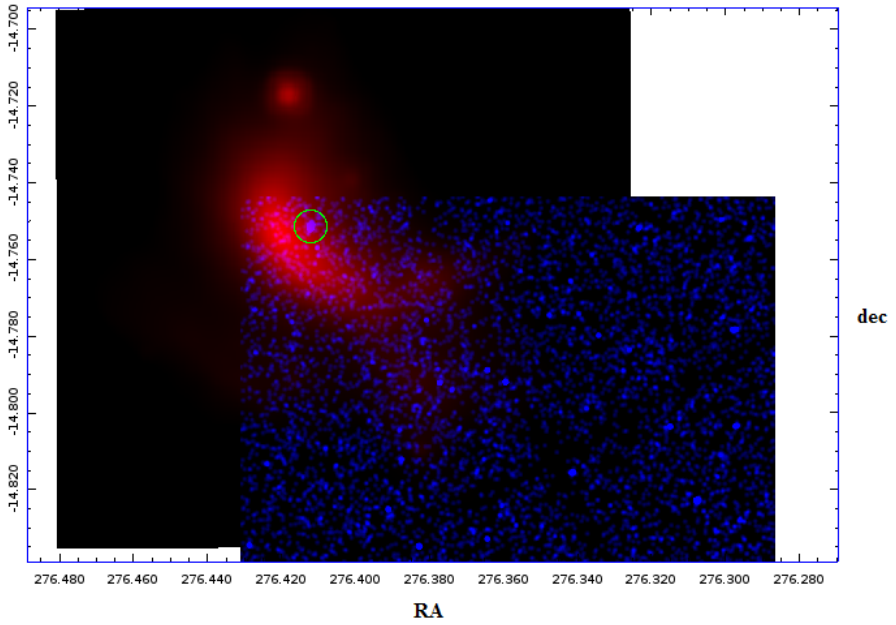

Figure 6.6: A broadband Chandra 0.2-8 keV image of the area around BD -14 5040 (in blue) overlaid on WISE 22 μm image (in red).

Since the source is relatively faint, I combined the spectra obtained from Obs IDs 4600 and 5341 for a better signal to noise ratio. Despite the agressive binning during the source extraction and combining the spectra, there were still a lot of bins that had zero or only few counts. This resulted in a faulty fit, with the model being systematically below the data. This was resolved by using alternative weighting, in my case Gehrels weighting, which works better if the number of counts in the bin is small.

Since the number of counts is small, χ-statistics and visual inspection of the fit are not useful methods for determining whether the fit is satisfactory. This was done using goodness-of-fit test. The expected absorbed powerlaw model (phabs(powerlaw)) matched poorly with the data. Instead, the most satisfactory model turned out to be an absorbed mekal model (equlibrium collisional plasma), frequently used to describe X-ray emissions from OB stars (Naze 2009[101]). The model gives the best-fit value of the column density $n_H \approx 1.1 \times 10^{22}\,\mathrm{cm}^{-2}$ and the plasma temperature approximately $kT \approx 0.22$ keV. Since the spectrum is not of high-quality, these values should be taken only as rough estimates. The obtained value for the plasma temperature is constistent with the temperatures of other OB stars[101] (e.g. Lopez-Santiago et al. (2012 [28]) derived $kT \approx 0.225$ keV for a similar main sequence star AE Aur).However, the most convincing evidence against the bow shock interpretation is that the X-ray emission is almost coincident to the position of BD -14 504.

The proximity of the X-ray source to BD -14 5040, its relatively small angular extent when compared to the bow shock itself, the spectrum which cannot be described using powerlaw models and good results obtained by using mekal models mean that it is almost certain that the X-ray emission is not associated with the observed infrared bow shock but rather with the star driving it.

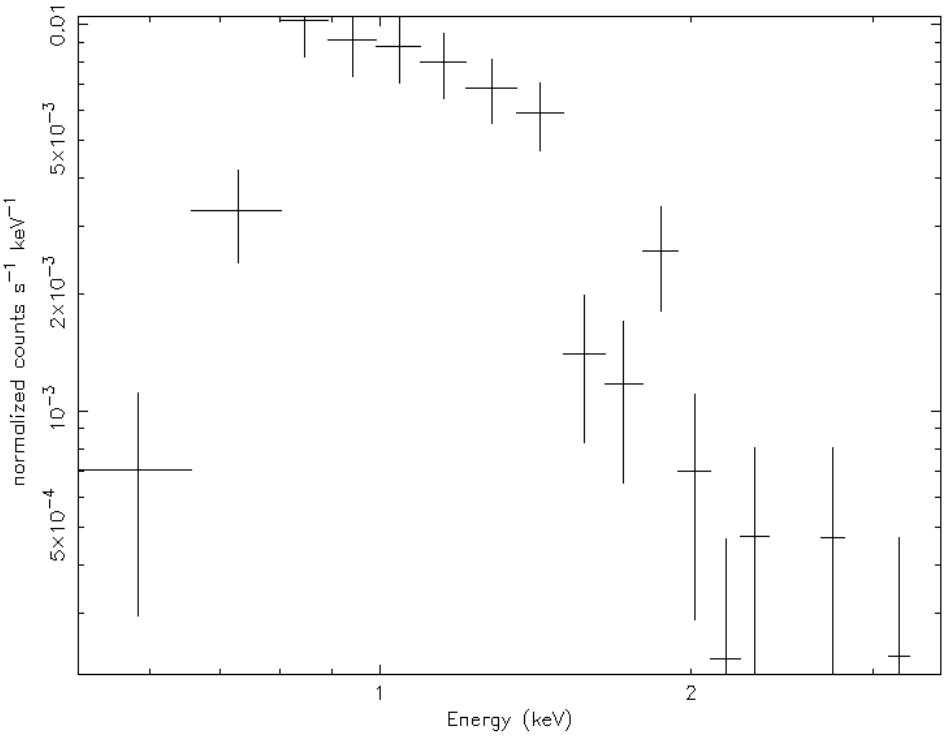

Figure 6.7: A spectrum of the compact X-ray source near the position of BD -14 5040. The spectrum was created by combining the individual spectra made from Obs IDs 4600 and 5341.

6.7 2MASS J17225002-3403223

2MASS J17225002-3403223 is a main sequence (B0 V) runaway from star-forming region NGC 6357 (add cite). By overlaying the WISE 22μm image on the Chandra broadband image of the region, no significant X-ray emission can be seen from within the bow shock (see Figure 6.8. To verify this, I extracted source counts from the region corresponding to the 22μm extended emission. Overall, there is no statistically significant count difference from the background, although there might be a slight soft X-ray excess within the bow shock. This excess is very small so no spectral study is possible (see Table 6.4).

band	count rate [10^{-3}s^{-1}]	S/B
broad	5.3 ± 3.0	1.3
soft	3.3 ± 1.6	1.9
med	0.8 ± 1.2	1.3
hard	1.3 ± 2.3	1.1

Table 6.4: Count estimates for the X-ray emission within the arcuate infrared nebula in the position of 2MASS J17225002-3403223.

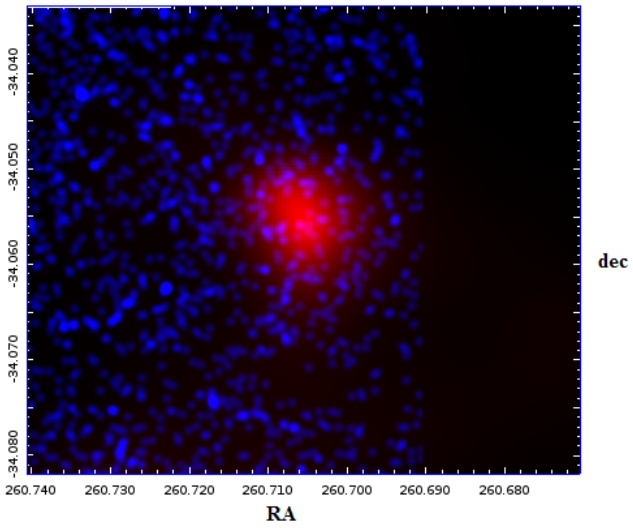

Figure 6.8: A broadband Chandra 0.2-8 keV image of the area around 2MASS J17225002-3403223 (in blue) overlaid on WISE 22 μm image (in red).

Chapter 7

Bow shocks and Strömgren spheres

Stellar bow shocks and Strömgren spheres are parsec-scale structures that can be detected at significant distances. Only a tiny fraction of stars form Strömgren spheres or stellar bow shocks, and even a smaller fraction forms them both. Such stars are very rare, but they are very interesting to study because of their high luminosity and peculiar velocity. The kinematic studies of such stars have relied on astrometry, either utilizing the catalog data or by doing a dedicated astrometrical study of a certain object by analysing images taken over a long time baseline. Such methods are often too cumbersome, and the catalog data may be incorrect. The kinematic studies of stars also rely on a precise knowledge of Galactic constants and the Solar peculiar motion, which are not known with high precision. Proper motion studies also do not give satisfactory results for objects with distances exceeding several kpc. In this section I present a method which enables us to determine the peculiar velocities of bow shock and Stromgren sphere-producing stars that may otherwise be out of reach of standard astrometric techniques.

7.1 Method

The Strömgren spheres and bow shocks had been used in past to investigate several stellar systems. For instance, Gvaramadze et al (2011 [11]) compared the values of number density of the ambient medium obtained from the parameters of the bow shock around Vela X-1 and from the radius of the Strömgren sphere present around the system. They report a good agreement. In a more recent paper, Gvaramadze et al. (2012 [102]) try to estimate the mass-loss rate of ζ Oph using its bow shock and Strömgren sphere. There exists a significant discrepancy between empirical and theoretical mass-loss rate of stars similar to ζ Oph, the so-called weak-wind problem. However, there are many stars, having both bow shocks and Strömgren spheres, with well-known stellar wind parameters but poorly known peculiar velocities. Here I propose a simple method to estimate peculiar velocities of such stars through observation of their bow shocks and Stromgren spheres. By rearranging the equation characterizing the Strömgren radius (see Chap. 2) we can obtain the expression for the gas number density:

$$n_H = \sqrt{\frac{3S(0)}{4\pi R_{st}^3 a^{(2)}}} \tag{7.1}$$

and plugging this into the equation for the minimum distance from the star at which the wind pressure is balanced by the ram and the thermal pressures of the ISM, the stand-off distance,

$$R_s = \sqrt{\frac{\dot{M} v_\infty}{4\pi n_H (\mu m_H v_\star^2 + 2kT)}} \tag{7.2}$$

where $\mu = 1.4$ is the mean molecular weight, m_H is the mass of a hydrogen atom, k is the Boltzmann constant and T ($\approx 10^4$ K) is the temperature of the ionized ISM, we get an equation giving the velocity of the star

$$v_\star^2 = \frac{\sqrt{a^{(2)}} R_{st}^{3/2} \dot{M} v_\infty}{\sqrt{3S(0)4\pi} R_S^2 \mu m_H} - \frac{2kT}{\mu m_H}. \tag{7.3}$$

It should be noted that this is merely an approximation, since the Strömgren spheres are far from perfectly spherical. I also assume that the tangential peculiar velocity of the star is much higher that its radial peculiar velocity.

7.2 Application to Vela X-1

Vela X-1 is one of a few high-mass X-ray binaries with an observable bow shock. Kaper et al. (1997[10]), who detected this bow shock for the first time, also note the presence of a H II region which they interpret as a Strömgren sphere with a radius of approximately 0.2 arcdeg. This corresponds to the physical radius of $R_{st} = 6.6$ pc considering the adopted distance to Vela X-1 of 1.9 kpc. The stand-off distance of the bow shock corresponds to $R_s = 0.5$ pc. The necessary parameters of Vela X-1 are given in Table 7.1.

Spectral type	B0.5 Iab
d [kpc]	1.9
v_∞ [km s^{-1}]	1100
$\dot{M}$ [10^{-6} M$_\odot$ yr^{-1}]	2
$(v_{tr})_{pec}$ [km s^{-1}]	38.7 ± 4.7
v_{pec} [km s^{-1}]	≈ 47

Table 7.1: Relevant parameters of Vela X-1 adopted from Gvaramadze et al. (2011 [11]) and [38]

The total ionizing-photon luminosity $S(0)$ of an B0.5 Iab star is not among the tabulated values that can be found in Lequeux (2005 [40]) or Martins, Schaerer & Hillier (2005 [103]). Instead, I use an approximate value $S(0) = 3 \times 10^{48}$photons s^{-1} given by Gvaramadze et al (2011 [11]). Assuming that the gas in the H II region is fully ionized and its temperature is $T = 10^4$ K, I can set the value for the recombination coefficient of hydrogen to all but the ground state to $a^{(2)} \approx 2.6 \times 10^{-13}$ cm^{3}s^{-1}. Using the method outlined above, I obtain the approximate value for the velocity of the system with respect to the surrounding ISM $v_\star \approx 32$km s^{-1}. It also needs to be taken into consideration that the value for the peculiar velocity of Vela X-1 was computed using only the errors in proper motion measurement (i.e. ignoring uncertainities in the distance to the system and the Galactic constants), so

one should take the error listed in Table 7.1 with caution, as it is its only the lower limit. Thus, it can be seen that the velocity $v_\star$ derived from the observation of the bow shock and Strömgren sphere associated with Vela X-1 is in excelent agreement with the value for the peculiar transverse velocity $(v_{tr})_{pec}$ computed from its proper motion.

7.3 Application to HIP 88652

HIP 88652 (HD 165319) is a bow shock-producing star thought to be expelled from a well-known open cluster NGC 6611, studied by Gvaramadze & Bomans (2008 [79]). The star shows very little or no proper motion (see Table 7.2), with measurement uncertainities comparable to the measurements themselves. Even when taking these measurements at face values, the computed peculiar tangential velocities are only of order ~ 10 km s^{-1}. These velocities are far lower than expected for runaway bow shock-producing stars.

Gvaramadze & Bomans also note that the star is located in the center of the H II region RCW158. They interpret this region as a Strömgren sphere created by the ultraviolet emission of the star. The Strömgren radius is about 12 arcminutes, which transforms (at the adopted distance of 2.0 kpc) into $R_{st} = 7.0$ pc. The bow shock stand-off radius was determined from the WISE images, R_s = 1.7 arcmin = 1.0 pc. As in the previous case, I assume full ionization of the gas and its temperature $T = 10^4$ K. Other parameters relevant for the calculations can be found in Table 7.3.

μ_α [mas/yr]	μ_δ [mas/yr]	catalogue
-0.2 ± 1.2	-1.0 ± 1.1	UCAC4 (Zacharias 2012)[88]
0.1 ± 0.8	-1.7 ± 0.6	PPMXL (Roser 2010)[90]
0.3 ± 1.0	-1.8 ± 0.6	NOMAD (Zacharias 2005)[91]

Table 7.2: Proper motions of HIP 88652

Spectral type	O9.5 Iab
d [kpc]	2.0
v_∞ [km s^{-1}]	2100
$\dot{M}$ [10^{-6} M$_\odot$ yr^{-1}]	5.3
$(v_{tr})_{pec}$ [km s^{-1}]	-
v_{pec} [km s^{-1}]	-

Table 7.3: Relevant parameters of HIP adopted from Gvaramadze & Bomans (tbd)

Adopting the total ionizing-photon luminosity of $S(0) = 4.9 \times 10^{48}$photons s^{-1} from Martins, Schaerer & Hillier (2005 [103]), I obtain the approximate value for the velocity of the system with respect to the surrounding ISM $v_\star \approx 34$km s^{-1}. Using a slightly larger value of $S(0) = 7.9 \times 10^{48}$photons s^{-1} from Lequeux (2005 [40]) translates into a smaller velocity $v_\star \approx 30$km s^{-1}.

Since there exists a discrepancy between these velocity estimates and tangential peculiar velocity inferred from the proper motion data, it is possible that the star itself does not possess a high peculiar velocity but fast large-scale flows of ISM in the vicinity of the star

can still produce a stellar bow shock. These flows are frequently produced by young open clusters. I querried the WEBDA service for any clusters in the proximity of HIP 88652 that could be sources of outflows capable of producing the observed bow shock orientation. However, there are no cataloged clusters near HIP 88652 that may influence the local ISM. It is likely that the observed bow shock is formed due to a high peculiar velocity of the star, however, the possible presence of fast ISM flows cannot be entirely dismissed.

The estimate of the peculiar velocity enables us to revisit some unresolved problems from Gvaramadze & Bomans, particularly concerning the kinematics of HIP 88652. Using the data provided in the Table 1. and Fig. 1. from Gvaramadze & Bomans, I estimate the position of the ejection site of HIP 88652 from the cluster to be approximately at $l = 16.5°$, $b = 1.0°$. This is about 2.65 arcdeg from the current position of HIP 88652. At the distance of 2 kpc, this translates into a linear distance of about 92 pc. Using the peculiar velocity computed from the proper motion, Gvaramadze & Bomans attempted to determine kinematic age (time elapsed since the ejection of HIP 88652 from NGC 6611) but this led to the values exceedding the age of the cluster itself (the age of NGC 6611 is about 4 Myr). Adopting my estimate of peculiar velocity $v_\star \approx 34\mathrm{km\,s^{-1}}$, I obtain the kinematic age of HIP 88652 $t_{kin} \approx 2.7$ Myr. The star was thus expelled during the early stages of the cluster evolution. Since these stages are dominated by the dynamical ejections of cluster members and the first supernova explosions begin to occur only when the cluster age exceeds 3 Myr, it is likely that HIP 88652 acquired its high peculiar velocity via a dynamical ejection from NGC 6611.

7.4 Discussion & future prospects

I emphasize that there is a slight difference in the peculiar velocities computed from the proper motion measurements and ones computed from the parameters of bow shocks and Strömgren spheres. While the peculiar velocity from the proper motion gives the velocity of the star with respect to its local standard of rest, the velocity derived from bow shocks and Strömgren spheres gives the motion of the star with respect to its surrounding ISM. This difference may be neglected in a lot of cases, especially when dealing with fast runaway or hypervelocity stars. However, problems may arise when studying the stars near some open clusters or associations that may give rise to ISM outflows with velocities comparable to those of typical runaway stars. Thus, the presence of such clusters and associations that may affect the state of the ISM near the star needs to be investigated and taken into the consideration before computing the peculiar velocity. On the other hand, it there are high-quality proper motion measurements available, this difference enables us to characterize the outflows of ISM themselves, especially for the closer clusters with multiple bow shock-producing systems in their vicinity.

It is quite hard to associate an uncertainity to the computed velocity. Since the method relies on a subjective visual determination of the radius R_{st} of the Strömgren sphere and some general assumptions about the ISM, it is hard to quantify. Since the R_{st} needs to be in the physical units, this method also relies on the precision of the distance measurements. Thus, some caution needs to be exercised when interpreting the results.

Despite these drawbacks and the obvious fact that this technique does not depend on proper motion measurements and thus it is unaffected by their uncertainities, it has several

advantages. Computing the peculiar motion of an object relies on the knowledge of the distance to the Galactic center and the rotational curve of the Galaxy, these parameters, especially the latter one, are ill-determined. It is even hard to associate an uncertainity with them. Thus, most authors in their research simply ignore those uncertainities when computing their peculiar velocities. Another strength of this technique is the sheer distance over which it can be applied. Using proper motion measurements, one can detect high-velocity stars within few kpc (the precise distance depends on the quality of the data, peculiar velocity of the star, time baseline of the measurement etc.). As of writing this thesis, there are several know bow shock-producing stars as far as the Large Magellanic Cloud (distance of about 50 kpc). This is more than 10 times further than the current limit of the proper motion-based techniques.

There are several new bow shocks found each year. This amount can be expected to increase further considering the vast amount of infrared data obtained by missions such as WISE or Spitzer stored in publicly accessible archives and advances in data processing. Furthermore, more advanced infrared missions such as The James Webb Space Telescope (JWST) will, without doubt, provide a more detailed view of the known bow shocks and uncover new ones as well. With more bow shocks and Strömgren spheres-producing sources, it can be expected that this method of estimating peculiar velocities will become even more potent in the future.

Chapter 8

Conclusion

In this work I have studied the stellar bow shocks driven by stars of early spectral types. In Chap. 1, I introduce bow shocks and show that bow shocks are ubiquitous in astrophysics, present in almost all scales ranging in sizes from fractions of AU (associated with planets) to several Mpcs (associated with galaxy clusters) and driven by a large variety of objects. I also list some of their interesting aspects and how they can be used to determine various properties of the objects that drives them and the properties of the surrounding medium as well. Chap. 2 focuses on the bow shock astrophysics in more detail, discussing their structure, morphologies and radiation. Some objects similar in appearance to the stellar bow shocks are also briefly discussed. Some background in Strömgren spheres is also included, since it will prove useful later in the text.

Chap. 3 starts the practical part of the thesis. Since this work uses data from the Spitzer Space Telescope, Wide-field Infrared Survey Explorer (WISE), Herschel Space Observatory and Chandra X-ray Observatory, I focus heavily on the instruments aboard these mission, methods of obtaining and handling the data and data reduction.

Chap. 4 describes the sample of the stellar bow shock compiled for this work and its data coverage by various instruments. I provide a higher-quality imagery made from the Spitzer data for bow shocks included in E-BOSS catalog which were previously covered only by the WISE images and use these higher-quality images to refine some bow shock characteristics and local ISM density estimates. I also investigate the deviations of the observed bow shocks from their prescribed shape and note that those deviations are significant for most of the cases in my sample. This means that using these analytical shapes when determining whether a certain arcuate mid-infrared feature is a stellar bow shock or not is not reliable. I search for a possible correlation between these deviations and stellar wind parameters of the stars driving the bow shocks, but no apparent correlation is visible in the data. There may exist a correlation between the nature of the outer layer of the bow shock (radiative or adiabatic) and the deviation of the bow shock from the analytical shape, however, higher-quality data are needed to reach a definite conclusion. Finally, I discuss and demonstrate the untapped potential of the Herschel Space Observatory, particularly its PACS instrument, for bow shock observations and provide several images of the bow shocks around high-mass X-ray binaries using the PACS data. I also compute the flux estimates in these bands and discuss how the dust masses within the bow shocks can be calculated and caveats associated with these calculations.

In Chap. 5, I present a candidate bow shock around the source 2MASS J17222408-3708484 that was discovered by accident when examining the field around another, previously studied, bow shock candidate. I discuss the shape of the candidate bow shock and compute the peculiar tangential velocities from the catalogued proper motion measurements for several possible distances. I ascertain that 2MASS J17222408-3708484 is, in fact, a star and find a possible remnants of an interstellar bubble. I note the possibility that the arc around 2MASS J17222408-3708484 may be a dust or a bow wave and not a stellar bow shock.

Chap. 6 deals with a possible X-ray emission produced by the stellar bow shocks using the data obtained by the Chandra X-ray Observatory. While some excess emission is detected in some cases, it is also shown that it can be attributed to the soft X-ray emission produced by the background and foreground stars, or the star driving the bow shock. I conclude that no bow shock X-ray emission has been detected using the Chandra data, however, there still exists an opportunity to utilize more sensitive (but having a worse spatial resolution) XMM Newton mission.

Finally, Chap. 7 proposes a simple method of determining stellar tangential peculiar velocities (or more precisely, the stellar velocity with respect to the surrounding medium) using the bow shock and Strömgren sphere morphologies. I investigate the viability of this method on Vela X-1 and achieve a good agreement between the velocities obtained from proper motion measurements and by the proposed method. Using this method, I also investigate the kinematic properties of the bow shock-driving star HIP 88652. The chapter is concluded by a brief discussion on the strengths and limitations of this method. Parsec-scale sizes of both bow shocks and Strömgren spheres may enable us to estimate the tangential peculiar velocities at considerable distances, far beyond the reach of the proper motion-based calculations. The situation may even improve with the advent of more modern infrared space missions planned for the near future.

Bibliography

[1] J.Llama, A. A. Vidotto, M. Jardine et al.: *Exoplanet Transit Variability: Bow Shocks and Winds Around HD 189733b*, preprint (2013).

[2] L. B. Wilson III: *The Microphysics of Collisionless Shocks*, A dissertation submitted to the faculty of the graduate school of the University of Minnesota (2010).

[3] J. G. J. van Oijen: *Are massive X-ray binaries runaway stars?*, A&A, **217**, 115-126 (1989).

[4] F. Huthoff, L. Kaper: *On the absence of wind bow-shocks around OB-runaway stars: Probing the physical conditions of the interstellar medium*, A&A, **383**, 999-1010 (2002).

[5] V. V. Gvaramadze, C. Weidner, P. Kroupa, J. Pflamm-Altenburg: *Field O stars: formed in situ or as runaways?*, MNRAS, **424**, 3037-3049.

[6] J. Silk, V. Antonuccio-Delogu, Y. Dubois et al.: *Jet interactions with a giant molecular cloud in the Galactic centre and ejection of hypervelocity stars*, A&A, **545**, L11 (2012).

[7] L. E. Palladino, K. J. Schlesinger, K. Holley-Bockelmann et al.: *Hypervelocity Star Candidates in the SEGUE G & K Dwarf Sample*, preprint (2013).

[8] M. Kilic, A. Gianninas, W. R. Brown. et al.: *The Runaway Binary LP 400-22 is Leaving the Galaxy*, MNRAS, **434**, 3582 (2013).

[9] C. S. Peri, A. T. Araudo, P. Benaglia et al: *ANALYSIS OF THE SPECTRAL ENERGY DISTRIBUTION FROM A RUNAWAY STAR BOW SHOCK*, RevMexAA (Serie de Conferencias), **40**, 156 (2011).

[10] Kaper, L., J. T. van Loon, T. Augusteijn et al.: *Discovery of a Bow Shock around Vela X-1*, ApJ, **475**, L37 (1997).

[11] V.V. Gvaramadze, S. Roser, R.-D. Scholz et al.: *4U 1907+09: an HMXB running away from the Galactic plane*, A&A, **529**, A14 (2011).

[12] L. Decin, N. L. J. Cox, P. Royer et al.: *The enigmatic nature of the circumstellar envelope and bow shock surrounding Betelgeuse as revealed by Herschel. I. Evidence of clumps, multiple arcs, and a linear bar-like structure*, A&A, **548**, A113 (2012).

[13] V. V. Gvaramadze, K. M. Menten, A. Y. Kniazev et al.: *IRC -10414: a bow-shock-producing red supergiant star*, MNRAS, Advance Access, 14 pp. (2013).

[14] B. M. Gaensler, P. O. Slane: *The Evolution and Structure of Pulsar Wind Nebulae*, ARAA, **44**, 17-47 (2006).

[15] B. M. Gaensler, S. Chatterjee, P. O. Slane et al.: *The X-Ray Structure of the Pulsar Bow Shock G189.22+2.90 in the Supernova Remnant IC 443*, AJ, **648**, 1037 (2006).

[16] Z. Wang, D. L. Kaplan, P. Slane et al.: *Serendipitous Discovery of an Infrared Bow Shock near PSR J1549-4848 with Spitzer*, AJ, **769**, 122 (2013).

[17] P. Hartigan, A. Frank, J. M. Foster et al.:*Fluid dynamics of stellar jets in real time: third epoch Hubble Space Telescope images of HH1, HH34 and HH 47*, AJ, **736**, 20pp (2011).

[18] P. F. Winkler, B. J. Williams, S. P. R. R. Petre et al.: *A high-resolution X-ray and optical study of SN 1006: asymmetric expansion and small-scale structure in a type Ia supernova remnant*, preprint (2013).

[19] M. A. Guerrero, J. A. Toala, J. J. Medina et al.: *Unveiling shocks in planetary nebulae*, preprint (2013).

[20] J. Meaburn, P. Boumis & S. Akras: *The bow-shock and high-speed jet in the faint, 40 arcmin diameter, outer halo of the evolved Helix panetary nebula (NGC 7293)*, preprint (2013).

[21] http://galex.stsci.edu/GalexView/

[22] P. Crumley & P. Kumar: *Radio emission from the bow shock of G2*, MNRAS, **436**, 1955 (2013).

[23] D. van Buren & R. McCray: *Bow shocks and bubbles are seen around hot stars by IRAS*, ApJ, **329**, L93 (1988).

[24] C. S. Peri, P. Benaglia, D. P. Brookes et al.: *E-BOSS: an Extensive stellar BOw Shock Survey. I. Methods and first catalogue*, A&A, **538**, A108 (2012).

[25] P. Hartigan, J. A. Morse, J. Tumlinson et al.: *Hubble Space Telescope Faint Object Spectrograph Optical and Ultraviolet Spectroscopy of the Bow Shock HH 47A*, ApJ, **512**, 901 (1999).

[26] D. C. Martin, M. Seibert, J. D. Neill et al.: *A turbulent wake as a tracer of 30000 years of Mira's mass loss history*, Nature, **448**, 780 (2007).

[27] Y. Terada, M. S. Tashiro, A. Bamba et al.: *Search for Diffuse X-Rays from the Bow Shock Region of Runaway Star BD +43 3654 with Suzaku*, PASJ, **64**, Article No.138 (2012).

[28] J. Lopez-Santiago, M. Miceli, M. V. del Valle et al.: *AE Aurigae: First Detection of Non-thermal X-Ray Emission from a Bow Shock Produced by a Runaway Star*, ApJ Letters, **757**, L6 (2012).

[29] M. V. del Valle & G. E. Romero: *Non-thermal processes in bowshocks of runaway stars. Application to ζ Ophiuchi*, A&A, **543**, A56 (2012).

[30] M. V. del Valle, G. E. Romero & M. De Becker: *Is the bowshock of the runaway massive star HD 195592 a Fermi source?*, A&A, **550**, A112 (2013).

[31] P. Benaglia, G. E. Romero, J. Mart et al.: *Detection of nonthermal emission from the bow shock of a massive runaway star*, A&A, **517**, L10 (2010).

[32] P. Benaglia, I. R. Stevens, & C. S. Peri: *Runaway stars: their impact on the intestellar medium*, BAAA, **55**, 165 (2012).

[33] V. B. Baranov, K. V. Krasnobaev & A. G. Kulikovskii: *A Model of the Interaction of the Solar Wind with the Interstellar Medium*, SPhD, **15**, 791 (1971).

[34] F. P. Wilkin: *Exact Analytic Solutions for Stellar Wind Bow Shocks*, APJ, **459**, L31 (1996).

[35] A. Schulz, M. Ackermann, R. Buehler et al.: *Systematic search for high-energy gamma-ray emission from bow shocks of runaway stars*, A&A, **565**, A95 (2014).

[36] Ochsendorf, B. B., Cox, N. L. J., Krijt, S. et al.: *Blowing in the wind: The dust wave around σ Orionis AB*, A&A, **563**, A65 (2014).

[37] Ochsendorf, B. B., Verdolini, S., Cox, N. L. J. et al.: *Radiation-pressure-driven dust waves inside bursting interstellar bubbles*, A&A, **566**, A75 (2014).

[38] M. Prisegen: *Study of high mass X-ray binaries*, A thesis submitted to Masaryk University Faculty of Science(2012).

[39] H. A. Kobulnicky, I. J. Gilbert & D. C. Kiminki: *OB Stars and Stellar Bow shocks in Cygnus-X: A Novel Laboratory Estimating Stellar Mass Loss Rates*, ApJ, **710**, 549 (2010).

[40] J. Lequeux: *The Interstellar medium*, Springer (2005).

[41] D. Maoz: *Basic Astrophysics*, Princeton University Press (2007).

[42] G. G. Fazio et al., ApJS, **154**, 10 (2004).

[43] J. R. Houck et al., ApJS **154**, 18 (2004).

[44] G. H. Rieke et al., ApJS, **154**, 25 (2004).

[45] http://irsa.ipac.caltech.edu/data/SPITZER/docs/spitzermission/missionoverview/spitzertelescopehandbook/.

[46] http://irsa.ipac.caltech.edu/data/SPITZER/docs/irac/iracinstrumenthandbook/.

[47] http://irsa.ipac.caltech.edu/data/SPITZER/docs/mips/mipsinstrumenthandbook/.

[48] http://irsa.ipac.caltech.edu/data/SPITZER/docs/dataanalysistools/tools/mopex/mopexusersguide/.

[49] http://irsa.ipac.caltech.edu/data/SPITZER/docs/dataanalysistools/cookbook/.

[50] E. L. Wright, P. R. M. Eisenhardt, A. K. Mainzer et al.: *The Wide-field Infrared Survey Explorer (WISE): Mission Description and Initial On-orbit Performance*, AJ, **140**, 1868 (2010).

[51] G. L. Pilbratt, J. R. Riedinger, T. Passvogel et al.: *Herschel Space Observatory - An ESA facility for far-infrared and submillimetre astronomy*, A&A, **518**, L1 (2010).

[52] A. Poglitsch, C. Waelkens, N. Geis et al.: *The Photodetector Array Camera and Spectrometer (PACS) on the Herschel Space Observatory*, A&A, **518**, L2 (2010).

[53] M. J. Griffin, A. Abergel, A. Abreu et al.: *The Herschel-SPIRE instrument and its in-flight performance*, A&A, **518**, L3 (2010).

[54] T. de Graauw, F. P. Helmich, T. G. Phillips et al.: *The Herschel-Heterodyne Instrument for the Far-Infrared (HIFI)*, A&A, **518**, L6 (2010).

[55] S. Ott: *The Herschel Data Processing System — HIPE and Pipelines — Up and Running Since the Start of the Mission*, ASP Conference Series, **434**, 139 (2010).

[56] K. Arnaud, R. Smith & A. Siemiginowska: *Handbook of X-ray Astronomy*, Cambridge, UK: Cambridge University Press (2011).

[57] D. A. Schwartz: *The Development and Scientific Impact of the Chandra X-Ray Observatory*, Int.J.Mod.Phys., **D13**, 1239 (2004).

[58] G. P. Garmire: *The Chandra X-ray observatory*, Bull. Astr. Soc. India, **39**, 225 (2011).

[59] A. Fruscione, J. C. McDowell, G. E. Allen et al.: *CIAO: Chandra's data analysis system*, SPIE Proc., **6270**, 62701V (2006).

[60] http://cda.harvard.edu/chaser/

[61] http://cxc.harvard.edu/ciao/threads/archivedownload/

[62] http://cxc.harvard.edu/ciao/ahelp/download_chandra_obsid.html

[63] http://cxc.harvard.edu/ciao/threads/intro_data/

[64] http://cxc.harvard.edu/ciao/threads/createL2/

[65] http://cxc.harvard.edu/ciao/ahelp/chandra_repro.html

[66] http://cxc.harvard.edu/ciao/threads/combine/

[67] http://cxc.harvard.edu/ciao/ahelp/reproject_obs.html

[68] http://cxc.harvard.edu/ciao/threads/true_color/

[69] http://cxc.harvard.edu/ciao/threads/source_counts/

[70] http://cxc.harvard.edu/ciao/ahelp/dmextract.html

[71] http://cxc.harvard.edu/ciao/threads/extended/

[72] http://cxc.harvard.edu/ciao/ahelp/specextract.html

[73] http://cxc.harvard.edu/ciao/threads/coadding/

[74] http://cxc.harvard.edu/ciao/ahelp/combine_spectra.html

[75] http://heasarc.gsfc.nasa.gov/xanadu/xspec/XspecManual.pdf

[76] K. A. Arnaud: *Astronomical Data Analysis Software and Systems V*, ASP Conf. Series, **101**, 17 (1996).

[77] H. A. Kobulnicky, M. J. Lundquist, A. Bhattacharjee et al.: *IRAS 03063+5735: A Bowshock Nebula Powered by an Early B Star*, AJ, **143**, 71 (2012).

[78] J. Ngoumou, T. Preibisch, T. Ratzka et al.: *The Mysterious Sickle Object in the Carina Nebula: A Stellar Wind Induced Bow Shock Grazing a Clump?*, ApJ, **769**, 139 (2013).

[79] V. V. Gvaramadze & D. J. Bomans: *Search for OB stars running away from young star clusters. I. NGC 6611*, A&A, **490**, 1071 (2008).

[80] V. V. Gvaramadze, A. Y. Kniazev, P. Kroupa et al.: *Search for OB stars running away from young star clusters. II. The NGC 6357 star-forming region*, A&A, **535**, A29 (2011).

[81] D. R. Gies & C. T. Bolton: *The binary frequency and origin of the OB runaway stars*, ApJS, **61**, 419 (1986).

[82] D. Ladjal, M. J. Barlow, M. A. T. Groenewegen et al.: *Herschel PACS and SPIRE imaging of CW Leonis*, A&A, **518**, L141, (2010).

[83] N. L. J. Cox, F. Kerschbaum, A.-J. van Marle et al.: *A far-infrared survey of bow shocks and detached shells around AGB stars and red supergiants*, A&A, **537**, A35 (2012).

[84] http://herschel.esac.esa.int/twiki/pub/Public/PacsCalibrationWeb/Balog_ExpAstr_2013.pdf

[85] M. F. Skrutskie, R. M. Cutri, R. Stiening et al.: *The Two Micron All Sky Survey (2MASS)*, AJ, **131**, 1163 (2006).

[86] L. D. Anderson, T. M. Bania, D. S. Balser et al.: *The WISE catalog of Galactic H II regions.*, ApJS, **212**, 1 (2014).

[87] *GLIMPSE Source Catalog (I + II + 3D)*, CDS/ADC Collection of Electronic Catalogues, **2293**, 0 (2009).

[88] N. Zacharias, C. T. Finch, T. M. Girard et al.: The fourth US Naval Observatory CCD Astrograph Catalog (UCAC4), AJ, **145**, 44 (2013).

[89] T. M. Girard, W. F. van Altena, N. Zacharias et al.: *The Southern Proper Motion program. IV. The SPM4 catalog.*, AJ, **142**, 15 (2011).

[90] S. Roeser, M. Demleitner & E. Schilbach, AJ, **139**, 2440 (2010).

[91] N. Zacharias, D. G. Monet & S. E. Levine: *Naval Observatory Merged Astrometric Dataset (NOMAD)*, San Diego AAS Meeting, January 2005. (2005).

[92] M.J. Reid, K. M. Menten, X. W. Zheng et al.: *A Trigonometric Parallax of Sgr B2*, ApJ, **705**, 1548 (2009).

[93] P. J. McMillan & j. J. Binney: *The uncertainty in Galactic parameters* , MNRAS, **402**, 934 (2010).

[94] T. G. Mdzinarishvili & K. B. Chargeishvili: *New runaway OB stars with HIPPARCOS*, A&A, **431**, L1- L4 (2005).

[95] T. M. Tauris: *Maximum speed of hypervelocity stars ejected from binaries*, preprint (2014).

[96] R. J. Simpson, M. S. Povich, S. Kendrew et al: *The Milky Way Project First Data Release: a bubblier Galactic disc.*, MNRAS, **424**, 2442 (2012).

[97] S. H. Pravdo, C. S. R. Day, L. Angelini et al.: *ASCA and GRO Observations of GX 301-2*, ApJ, **454**, 872 (1995).

[98] T. Endo, M. Ishida, K. Masai et al.: *Broadening of Nearly Neutral Iron Emission Line of GX 301-2 Observed with ASCA*, ApJ, **574**, 879 (2002).

[99] http://adsabs.harvard.edu/abs/2002cxo..prop.1179E.

[100] C. B. Reed: *Catalog of Galactic OB Stars*, AJ, **125**, 2531 (2003).

[101] Y. Naze: *Hot stars observed by XMM-Newton. I. The catalog and the properties of OB stars*, A&A, **506**, 1055 (2009).

[102] V. V. Gvaramadze, N. Langer & J. Mackey: *ζ Oph and the weak-wind problem*, MNRAS: Letters, **427**, L50 (2012).

[103] F. Martins, D. Schaerer & D. J. Hillier: *A new calibration of stellar parameters of Galactic O stars*, A&A, **436**, 1049 (2005).